

Tunability in Heterobimetallic Complexes Featuring an Acyclic “Tiara” Polyether Motif

Joseph P. Karnes, Natalie M. Lind, Allen G. Oliver, Cynthia S. Day, Victor W. Day, and James D. Blakemore*



Cite This: *Inorg. Chem.* 2025, 64, 571–593



Read Online

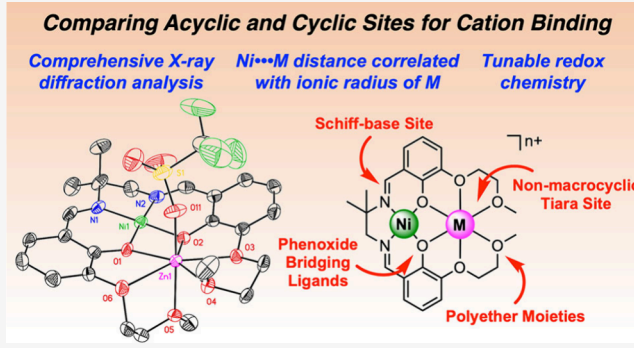
ACCESS |

Metrics & More

Article Recommendations

Supporting Information

ABSTRACT: Both cyclic “crown” and acyclic “tiara” polyethers have been recognized as useful for the binding of metal cations and enabling the assembly of multimetallic complexes. However, the properties of heterobimetallic complexes built upon acyclic polyethers have received less attention than they deserve. Here, the synthesis and characterization of a family of eight redox-active heterobimetallic complexes that pair a nickel center with secondary redox-inactive cations (K^+ , Na^+ , Li^+ , Sr^{2+} , Ca^{2+} , Zn^{2+} , La^{3+} , and Lu^{3+}) bound in acyclic polyether “tiara” moieties are reported. Structural studies with X-ray diffraction analysis were carried out on the monometallic nickel precursor complex to the heterobimetallics and the adducts with K^+ , Li^+ , Sr^{2+} , Zn^{2+} , and Lu^{3+} ; the results confirm the binding of secondary cations in the tiara site and demonstrate that the tiara moiety is more conformationally flexible than the analogous 18-crown-6-like moiety of a closely related macrocyclic “crown” ligand. Spectroscopic and electrochemical studies show, however, that the stability and cation-driven tunability of the tiara-based heterobimetallic species are quite similar to those previously measured for crown-based species. Consequently, the tiara motif appears to be at least as equally useful for constructing tunable multimetallic species as the more commonly encountered crown motif; a comprehensive set of titration data collected in an acetonitrile solution support this conclusion as well. Because the use of acyclic tiaras avoids the need for tedious and/or time-intensive syntheses of macrocyclic structures, these findings suggest that tiara motifs could be broadly advantageous in the design of ligands to support multimetallic chemistry.



Downloaded via UNIV OF KANSAS on August 6, 2025 at 15:25:07 (UTC).
See https://pubs.acs.org/sharingguidelines for options on how to legitimately share published articles.

useful of these ligands display tight binding of cations, overcoming cation–cation repulsion and the natural tendency for metal cations to form multiple species in solution. Orthogonal metalation behavior in which each metal cation is incorporated into a specific, addressable site of given ligand is also quite useful, as it enables study of families of complexes that differ only in the identity of the incorporated secondary metal cation rather than also with regard to the site in which the cations bind. One class of macrocycles that displays these attractive properties was developed by Reinhoudt and co-workers in the 1980s.¹⁸ These heteroditopic macrocycles feature a Schiff-base binding site that favors the binding of various metals, often of a redox-active nature, and an appended crown-ether-like site that can tightly bind secondary cations. A

INTRODUCTION

The incorporation of secondary metal cations into parent metal-containing complexes is a proven and reliable method for tuning of inorganic/organometallic molecular properties. Achieving tunability attracts significant interest in studies of redox chemistry,^{1–4} molecular catalysis,^{5–10} and spectroscopy,^{11–13} and thus much effort has been devoted in recent years to quantifying and understanding the origins of tuning effects engendered by incorporation of secondary metal cations. Studies in this realm have primarily focused on the role of cation identity in promoting tunability. The charge, ionic radius, and Lewis acidity of cations have all been considered in parametrizations of cation-driven tuning effects, as have concepts such as cation-induced electric fields,¹⁴ cation-driven structural deformations,¹⁵ and size-dependent behaviors.^{5,16} Consequently, there is now a rich appreciation of the role of cations in modulating the properties of multimetallic species.¹⁷

The incorporation of secondary metal cations into tunable multimetallic species is usually achieved, however, through use of tailored heterotopic ligands. Heterotopic ligands present multiple sites in which metal cations can bind, and the most

Received: August 6, 2024

Revised: October 3, 2024

Accepted: November 7, 2024

Published: December 23, 2024

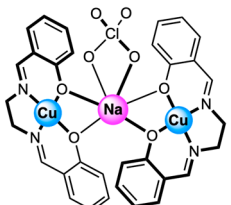


variety of systems have been explored on the Reinhoudt-type ligand platforms,^{12,14,19–21} including three families of homologous complexes developed by our group that feature Group 10 metals (Ni^{2+} , Pd^{2+} , and Pt^{2+}) in the Schiff-base site.^{22–24} We recently reported studies of the heterogeneous electron-transfer (ET) kinetics of the nickel species from this broader series of complexes.²²

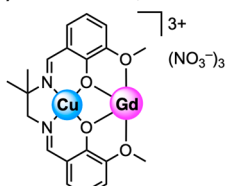
Nonmacrocyclic, heteroditopic ligands that are structural analogues of the Reinhoudt-type systems have also been studied (Chart 1). Important and early structural observations

Chart 1. Examples of Nonmacrocyclic Heterobimetallic Complexes:^a (a) Classic Work of Truter and Co-workers Showing the Association of a Sodium Cation with Copper Schiff-Base Complexes;²⁵ (b) Ether-Promoted Formation of a Discrete $[\text{Cu},\text{Gd}]$ Complex;³² (c) Acyclic Polyether-Promoted Formation of Tunable $[\text{Ni},\text{M}]$ Complexes;⁵ (d) Binding of Secondary Cations in an Acyclic Polyether Designed by Soo and Co-workers;³³ (e) Series of “Tiara” Complexes Reported Here

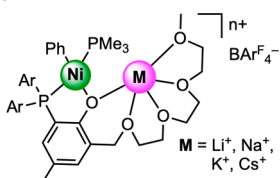
(a) *Truter and co-workers, 1968*



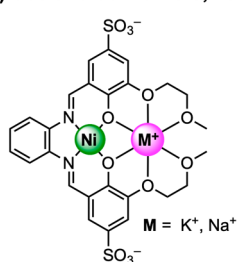
(b) *Costes et al., 1996*



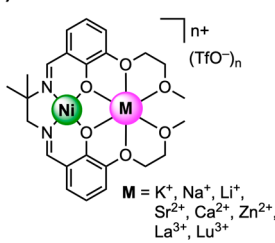
(c) *Do and co-workers, 2020*



(d) *Soo and co-workers, 2016*



(e) *This Work*



^aThis chart includes selected authors and years of publication for the chosen examples.

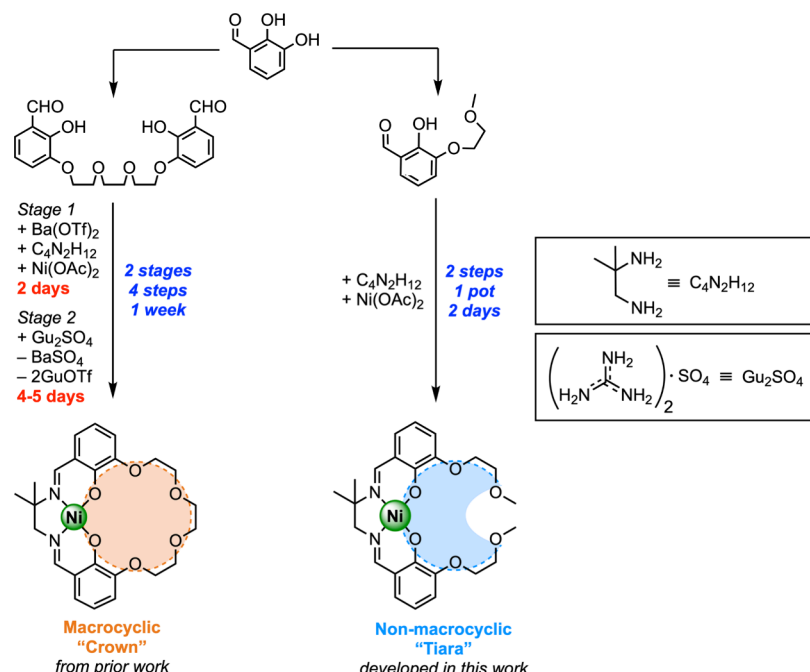
made by Milburn, Truter, and Vickery showed that a trinuclear phenoxide-bridged species could be formed between two equivalents of a Schiff-base copper(II) complex and one equivalent of sodium perchlorate, suggesting that anionic character at the phenoxide O atoms was sufficient to favor the assembly of multinuclear species.²⁵ Building on this early work, a range of alkoxy-substituted Schiff-base complexes have been developed that enable the formation of heterobimetallic species in which secondary cations are bound in tetradentate sites formed at the periphery of Schiff-base cores. Ghosh and co-workers have used such ligands in a number of attractive applications.^{26,27} Complexes of this type have been studied extensively in the solid state, including studies of magnetic

properties that depend on the identity of the incorporated secondary cation; the literature in this area suggests that not all the systems developed and studied to date are stable in the solution phase.^{28–31} This sensitivity is reasonable, however, in light of the solvation properties of electropositive metal cations in coordinating media.^{11,12} Considering all this, some parallels can be made between the properties of nonmacrocyclic Schiff-base ligands and Reinhoudt-type macrocycles, but such systems have usually differed in the number of chelating donor atoms and studies from several groups have examined reactivity and properties under distinct conditions in each case, precluding detailed comparisons.

However, beginning in 2016, Soo and co-workers developed a ligand concept that represents a very close nonmacrocyclic structural analogue of the Reinhoudt-type heteroditopic macrocycles that have proven so broadly useful for the preparation of heterobimetallic complexes.^{33–35} In the ligands from Soo and co-workers, Schiff-base cores containing Ni(II) were appended with chelating ether moieties, affording monometallic Ni(II) precursors that could interact with secondary monovalent cations such as Na^+ and K^+ , as shown through studies of cation-modulated catalytic hydrogen evolution. However, structures of only the monometallic Ni(II) complexes and their related derivatives incorporating KPF_6 were prepared in the work with these systems, precluding the establishment of a robust structural basis upon which to interpret how the unusual polyether site in these complexes enables cation binding. We also note here that some closely related heterobimetallic complexes featuring transition metal/s-block metal combinations have recently appeared, and that these have demonstrated benefits in catalysis compared with close macrocyclic analogues.³⁶

On the one hand, the ligands from Soo and co-workers are very similar to those developed by Reinhoudt and co-workers, from the perspective that they both feature tetradentate Schiff-base sites appended with nearby hexadentate polyether sites. Both systems also feature phenoxide ligands that can bridge between metal centers and enable the formation of $[\text{Ni}^{II}(\mu_2\text{-O}_{\text{phenoxide}})_2\text{M}^{n+}]$ cores. On the other hand, they differ in that the Reinhoudt-type ligands feature a *cyclic polyether ring* that usually resembles an 18-crown-6-like moiety formed by macrocyclization during synthesis. The ligands from Soo feature *acyclic polyether “arms”* that are formed under operationally simpler synthetic conditions prior to the assembly of the final ligand. Nonetheless, both the cyclic and acyclic ligands feature six oxygen donor atoms in the polyether site, making direct comparison of these systems quite attractive. Along this line, we anticipated that comprehensive studies of heterobimetallic complexes built on an acyclic platform would afford the opportunity to better understand how the macrocyclic, or nonmacrocyclic, nature of a ligand system impacts studies of multimetallic chemistry. Further, we anticipated that incorporating mono-, di-, and trivalent secondary cations would offer the opportunity to judge ligand behaviors with a suitably broad range of cations to make general conclusions about their behaviors.

Here, we report the synthesis, isolation, and study of a family of heterobimetallic nickel complexes built upon an acyclic, heteroditopic ligand framework. The incorporation of a range of secondary metal cations was carried out (K^+ , Na^+ , Li^+ , Sr^{2+} , Ca^{2+} , Zn^{2+} , La^{3+} , and Lu^{3+}), and results from single-crystal X-ray diffraction (XRD) analysis confirmed the assembly of $[\text{Ni}^{II}(\mu_2\text{-O}_{\text{phenoxide}})_2\text{M}^{n+}]$ cores in all cases for which suitable

Scheme 1. Synthetic Scheme Comparing the Routes for the Preparation of $[\text{Ni}]^T$ (Right) and $[\text{Ni}]^C$ (Left)^a

^aThe “tiara” $[\text{Ni}]^T$ can be prepared more quickly and easily than the “crown” $[\text{Ni}]^C$. The 2-day timeframe quoted for the preparation of $[\text{Ni}]^T$ from the derivatized aldehyde is based on the 20 h reaction time (see the Experimental Section) plus time for workup and characterization. OTf is the triflate anion (trifluoromethanesulfonate, CF_3SO_3^-).

crystals could be grown ($\text{M} = \text{K}^+$, Li^+ , Sr^{2+} , Zn^{2+} , and Lu^{3+}). Along with results for the corresponding monometallic nickel precursor, the structural data were used to establish an understanding of how the ligand studied here that features an acyclic polyether site, dubbed a “tiara” moiety, differs from more commonly studied ligands that feature cyclic “crown” polyether moieties. The term “tiara” was selected because of the structural relationship of the acyclic polyether moiety developed here with the more well recognizable cyclic “crown” systems studied in prior work. “Crown” and “tiara”, as terms, both refer to diadems that reflect dignity, sovereignty, or authority; a crown, however, is conventionally formed from a closed loop, while a tiara is formed by an unclosed band. In both ligand systems developed here, the positions adopted by the secondary cations depend on their ionic radii, but in the case of the tiara complexes, the smaller secondary cations can approach more closely to the nickel metal center. The latter feature is attributable to greater flexibility in the polyether site in the case of the tiara system. Spectroscopic and electrochemical studies were used to probe the cation-driven tunability of the tiara-based species, and the similarities and differences in the tuning behavior with prior results for the crown-based analogue are discussed here as well.

RESULTS

Synthesis and Characterization. Divergent synthesis is a useful strategy for the preparation of heterobimetallic complexes. In divergent synthesis, a monometallic precursor complex can be prepared, and then subsequently metalated with appropriate salts of secondary metal cations. With this strategy, many derivatives incorporating a wide range of secondary cations can be prepared, avoiding the need for convergent methods in which heterobimetallic species are isolated in a piecemeal fashion with sometimes widely varying

synthetic conditions being required.^{2,14} In prior work, we have found that divergent synthetic protocols enable the rapid preparation of families of heterobimetallic nickel complexes; we have explored two Reinhoudt-type macrocyclic ligands (denoted as $\text{H}_2\text{L}^{\text{salben}}$ and $\text{H}_2\text{L}^{\text{salmen}}$) that feature 18-crown-6 like moieties for the binding of secondary metal cations.^{12,20,22–24} However, divergent synthesis of the heterobimetallic complexes based on $\text{H}_2\text{L}^{\text{salben}}$ and $\text{H}_2\text{L}^{\text{salmen}}$ does not avoid the inherently time-intensive nature of assembling the macrocyclic ligands themselves. In the case of $\text{H}_2\text{L}^{\text{salmen}}$, which is most closely related to the work described here,²² a synthetic protocol composed of two stages and four individual steps is required to assemble the monometallic complex, representing an investment of approximately one total week of time (Scheme 1). This synthesis builds from commercially available salicylaldehyde, however, and leads to the quite useful monometallic complex that we denote here $[\text{Ni}]^C$ where the superscripted C indicates the presence of the crown-ether-like moiety in the isolated complex, making it suitable as a starting material for divergent metalation.

Inspired by many useful features of the synthesis of $[\text{Ni}]^C$ as originally reported by Reinhoudt and co-workers,^{18,22} we developed a synthetic route here for the preparation of the analogous yet nonmacrocyclic $[\text{Ni}]^T$. As shown Scheme 1, the synthetic pathway for $[\text{Ni}]^T$ is economical from both the standpoint of requiring fewer operational steps and requiring only 2 days to complete. The primary point of differentiation between the syntheses (Scheme 1) is the use of an abbreviated polyether-containing precursor, prepared according to a method similar to that used by Reinhoudt to generate the lariat ether needed for the preparation of $[\text{Ni}]^C$.^{33,37,38} A total of 2 equiv of this polyether-containing salicylaldehyde derivative was incorporated into the final monometallic complex with the goal of forming a new site that would be

poised for the binding of secondary metal cations. $[\text{Ni}]^{\text{T}}$ was thus prepared (see the *Experimental Section* for details) and isolated. Single crystals suitable for XRD analysis were grown, and as predicted from nuclear magnetic resonance (NMR) data (Figures S1 and S2), the nickel center adopts a square-planar geometry, coordinating to the Schiff-base site and not the O atoms of the polyether “arms” (Figure 1). The complex

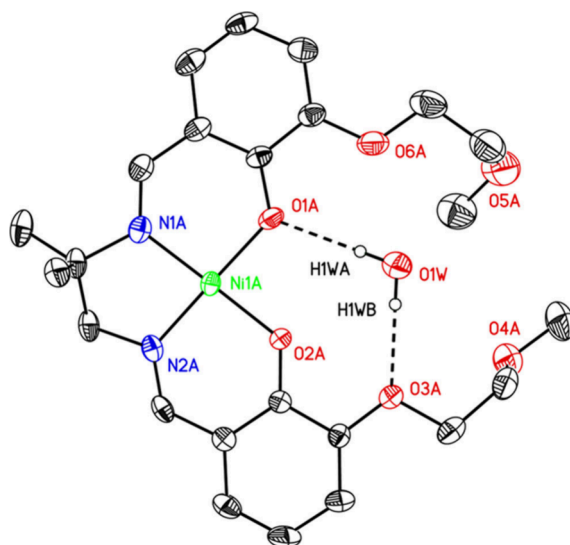


Figure 1. Solid-state structure (XRD) of $[\text{Ni}, \text{H}_2\text{O}]^{\text{T}}$. All minor components of disorder and all hydrogen atoms except those bonded to O1W are omitted for clarity. Displacement ellipsoids are shown at the 50% probability level.

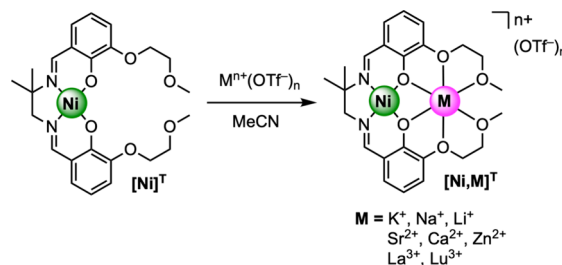
is overall neutral in the structure from XRD but features one cocrystallized molecule of water bound in the polyether site. ^1H NMR data suggest that $[\text{Ni}]^{\text{T}}$ can be fully dried under vacuum, in line with synthetic results for the bimetallic complexes as well (*vide infra*). However, $[\text{Ni}]^{\text{T}}$ is quite hygroscopic; elemental analysis data indicate that the sample of the complex sent for analysis took up ca. 0.5 equiv of H_2O en route to the facility that carried out the analysis. Considering all this, we denote the actual species that was crystallized and incorporates H_2O as $[\text{Ni}, \text{H}_2\text{O}]^{\text{T}}$.

The XRD structure of $[\text{Ni}, \text{H}_2\text{O}]^{\text{T}}$ reveals that, as desired, the two incorporated polyether ligand “arms” and the two phenoxide oxygen atoms are appropriately oriented to form a nascent cavity that could bind secondary metal cations. This nascent site features a total of six oxygen atoms that could serve as ligands for metal cations, making it analogous the 18-crown-6-like site of $[\text{Ni}]^{\text{C}}$. In $[\text{Ni}, \text{H}_2\text{O}]^{\text{T}}$, however, the ethylene bridge that would connect oxygen atoms O4A and O5A in the crystal structure has been removed, leading to an additional degree of freedom in the structure. We were inspired to term the moiety developed here as a “tiara” because the terms “crown” and “tiara” are related, both referring to diadems that reflect dignity, sovereignty, or authority; a crown is conventionally formed from a closed loop, but a tiara is usually an unclosed band. As the tiara is unclosed, the overall complex $[\text{Ni}]^{\text{T}}$ is overall nonmacrocyclic in nature; this difference simplifies the synthetic protocols significantly. No barium template is needed to form $[\text{Ni}]^{\text{T}}$, and no removal of barium is needed to access the monometallic final product. Removal of barium to form $[\text{Ni}]^{\text{C}}$, although a remarkably useful reaction developed by Reinhoudt and co-workers, adds

significant time (4–5 days) to the synthetic procedure needed to access the final $[\text{Ni}]^{\text{C}}$. In our route, $[\text{Ni}]^{\text{T}}$ can be isolated on the gram scale in just 2 days (see the *Experimental Section* for details).

With $[\text{Ni}]^{\text{T}}$ in hand, heterobimetallic complexes of the form $[\text{Ni}, \text{M}]^{\text{T}}$ were prepared by reaction of triflate salts of the desired secondary metal cations with $[\text{Ni}]^{\text{T}}$ in acetonitrile (MeCN). Specifically, 1 equiv of the triflate salts of K^+ , Na^+ , Li^+ , Sr^{2+} , Ca^{2+} , Zn^{2+} , La^{3+} and Lu^{3+} was reacted with $[\text{Ni}]^{\text{T}}$ to obtain 1:1 Ni:M bimetallic complexes with high yields in each case (Scheme 2). As in previous work, we have chosen to use

Scheme 2. Synthetic Scheme for the Preparation of the Heterobimetallic Complexes



the pK_a values of the metal-aqua complexes of the secondary cations as a measure of the effective Lewis acidities of these cations.³⁹ The cations used here span a wide range of Lewis acidities; the pK_a of K^+ is 16.0, and the pK_a of Lu^{3+} is 7.9. Here, we have expanded the number of cations explored as compared to our previous study of the $[\text{Ni}]^{\text{C}}$ system,²² in order to test the hypothesis that the tiara ligand system, with more degrees of freedom than the analogous crown, has the ability to bind smaller cations, such as Li^+ and Zn^{2+} , which are usually a poor size match for 18-crown-6 moieties. ^1H , $^{13}\text{C}\{^1\text{H}\}$, and ^{19}F NMR studies confirmed the formation of the desired heterobimetallic compounds in each case (Figures S3–S26), with no peak broadening or unusual chemical exchange behavior detectable even in the cases of the smallest cations Li^+ and Zn^{2+} . As expected, the ^1H NMR results for the tiara complexes $[\text{Ni}, \text{M}]^{\text{T}}$ for which we have previously prepared the analogous $[\text{Ni}, \text{M}]^{\text{C}}$ complexes (K^+ , Na^+ , Sr^{2+} , Ca^{2+} , La^{3+} , and Lu^{3+}) showed similar spectral profiles in both cases. The ^1H NMR spectra for the $[\text{Ni}, \text{M}]^{\text{T}}$ complexes are distinguished from those for the $[\text{Ni}, \text{M}]^{\text{C}}$ complexes, however, by the resonance(s) attributable to the two terminal methyl groups on the polyether “arms” of the $[\text{Ni}]^{\text{T}}$ framework that appear in place of the single resonance for the geometrically related methylene protons of the corresponding ethylene bridge present in the $[\text{Ni}]^{\text{C}}$ framework (Figures S3, S6, S9, S12, S15, S18, S21, and S24).²² In the spectra of $[\text{Ni}, \text{Ca}]^{\text{T}}$, $[\text{Ni}, \text{La}]^{\text{T}}$, and $[\text{Ni}, \text{Lu}]^{\text{T}}$, the methyl groups are not chemically equivalent and appear as two equally intense peaks (two resonances corresponding to 3H each; Figures S15, S21, and S24), but in all the other heterobimetallic species, the two methyl groups appear chemically equivalent (one resonance corresponding to 6H). In accordance with these spectroscopic findings, elemental analysis results also confirmed the composition and homogeneity of samples of the heterobimetallic complexes in all cases (see the *Experimental Section*). No evidence of cation scrambling between the individual metal-binding sites was observed for any of the $[\text{Ni}, \text{M}]^{\text{T}}$ complexes, and the desired heterobimetallic com-

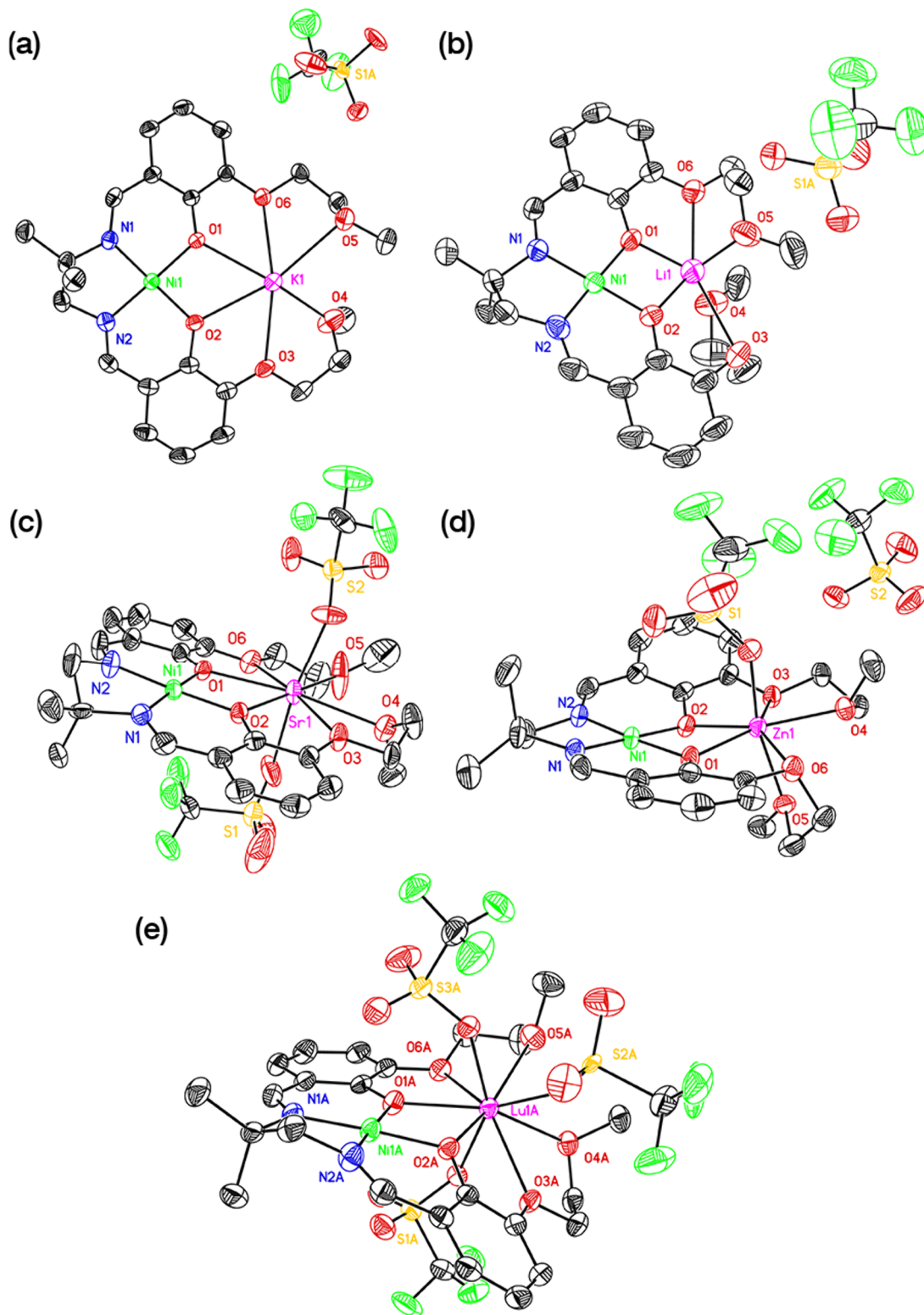


Figure 2. Solid-state structures of the heterobimetallic complexes obtained via single-crystal XRD experiments in this study: (a) $[\text{Ni},\text{K}]^T$; (b) $[\text{Ni},\text{Li}]^T$; (c) $[\text{Ni},\text{Sr}]^T$; (d) $[\text{Ni},\text{Zn}]^T$; (e) $[\text{Ni},\text{Lu}]^T$. All hydrogen atoms, outer-sphere cocrystallized solvent, and atoms associated with minor components of structural disorder are omitted for clarity. Displacement ellipsoids are shown at the 50% probability level in all cases with the exception of those for $[\text{Ni},\text{Sr}]^T$, which are shown at the 20% level for clarity.

plexes were obtained in good-to-excellent yields in each case (95–100%), confirming that the ligand system developed here supports orthogonal metalation and divergent synthesis, despite its nonmacrocyclic nature. This is attributable to covalent bonding between nickel and the four donor atoms in

the Schiff-base site, as well as the preference of nickel(II) to adopt a square-planar geometry.

Single-Crystal XRD Analysis. XRD analysis of the heterobimetallic complexes containing K^+ , Li^+ , Sr^{2+} , Zn^{2+} , and Lu^{3+} confirmed the assembly of the desired $[\text{Ni}^{\text{II}}(\mu_2$

Table 1. Comparisons of Notable Structural Parameters across the $[\text{Ni},\text{M}]^{\text{T}}$ Family Obtained via the Study of the XRD Data

compound	$[\text{Ni},\text{H}_2\text{O}]^{\text{T}}$	$[\text{Ni},\text{K}]^{\text{T}}$	$[\text{Ni},\text{Li}]^{\text{T}}$	$[\text{Ni},\text{Sr}]^{\text{T}}$	$[\text{Ni},\text{Zn}]^{\text{T}}$	$[\text{Ni},\text{Lu}]^{\text{T}}$
$\text{p}K_{\text{a}}$ of $[\text{M}(\text{H}_2\text{O})_m]^{n+}$ ^a		16.0	13.8	13.2	9.0	7.9
CN of M		7	6	8/9	7	9
Shannon ionic radius of M ^b		1.46	0.76	1.26 (CN = 8)	0.82 ⁱ	1.03
O1···O2 (Å)	2.531(8) ^h	2.519(3)	2.442(4)	2.501(7)	2.380(4)	2.418(4) ^j
O3···O6 (Å)	5.343(3)	5.302(3)	5.255(5)	5.355(9)	4.613(4)	4.807(5) ^j
N1···N2 (Å)	2.517(6) ^h	2.529(3)	2.535(5)	2.52(1)	2.547(6)	2.53(1) ^j
Ni–N _{imine} (Å) ^c	1.852(4) ^h	1.853(3)	1.846(3)	1.846(7)	1.838(4)	1.844(6) ^j
Ni–O _{phen} (Å) ^c	1.866(6) ^h	1.854(2)	1.846(3)	1.856(5)	1.836(3)	1.847(3) ^j
M–O _{phen} (Å) ^c		2.678(2)	2.005(8)	2.555(5)	2.106(3)	2.297(7) ^j
M–O _{3,6} (Å) ^c		2.738(2)	2.722(9)	2.680(6)	2.380(3)	2.526(6) ^j
M–O _{4,5} (Å) ^c		2.836(3)	1.96(1)	2.684(9)	2.150(3)	2.464(7) ^j
Ni···M (Å)		3.7038(8)	2.979(8)	3.600(1)	3.1032(8)	3.343(6) ^j
ω_{salmen} (Å) ^d	0.070 ^h	0.094	0.051	0.045	0.004	0.066 ^j
ω_{tiara} (Å) ^e	0.255 ^h	0.534	0.908 (0.026 ^j)	0.124	0.740 (0.074 ^m)	0.634 ^j
τ_4 (Å) ^f	0.062 ^h	0.082	0.052	0.041	0.052	0.068 ^j
ψ_{Ni} (Å) ^g	0.010 ^h	0.005	0.008	0.003	0.009	0.004 ^j
χ (deg) ^k	8.0 ^h	20.0	6.6	5.0	29.5	40.3 ^j

^aFrom ref 39. ^bFrom ref 41. For comparison, the ionic radius of nickel(II) with CN = 4 is 0.55 Å. ^cDefined as the average interatomic distances between the noted metal and the relevant oxygen/nitrogen atoms. ^dDefined as the RMSD of the positions of the O_{phen} and N_{imine} atoms from the mean plane of their positions. ^eDefined as the RMSD of the positions of the atoms O1–O6 from the mean plane of their positions. ^fGeometry index for four-coordinate complexes, with a value of 1.00 indicating perfect tetrahedral geometry and zero indicating perfect square-planar geometry. Calculated as described in ref 42. ^gAbsolute value of the distance between Ni and the mean plane of O1, O2, N1, and N2. ^hValues for $[\text{Ni},\text{H}_2\text{O}]^{\text{T}}$ correspond to the parameters for the major species in the structural data. See Table S4 for data regarding the independent molecular species. ⁱValue used for the Shannon ionic radius of the seven-coordinate Zn²⁺ ion was calculated as the arithmetic mean of the known radius values corresponding to six- and eight-coordinate Zn²⁺ ions from ref 41. ^jValues for $[\text{Ni},\text{Lu}]^{\text{T}}$ are given as the arithmetic mean of the values of the parameters for molecules A and B in the structural data. Stated e.s.d.'s on the distances were taken as the largest among the individual values corresponding to the independent molecular species in the refined structural data. See Table S5 for data regarding the independent molecular species. ^kDefined as the fold angle between the mean planes calculated for the two pseudoplanar [O₂C₇] moieties found in each structure; one contains O1, O6, and C1–C7 and the other contains O2, O3, and C14–C20. ^lDefined as the RMSD of the positions of the atoms O1, O2, O3, and O6. ^mDefined as the RMSD of the positions of the atoms O1, O2, O3, O4, and O6.

$\text{O}_{\text{phenoxide}})_2\text{M}^{n+}$] cores in each case. Similar to the prior series of complexes $[\text{Ni},\text{M}]^{\text{C}}$, in this new series of structures, the Ni(II) ion remains bound in the Schiff-base cavity; the secondary metal cations interact in each complex with the bridging phenoxide oxygen atoms as well as all of the ethereal oxygen atoms (see Figure 2 for images of the heterobimetallic structures). Refinement of the occupancy factors of the secondary metals as well as nickel confirmed selective binding in the polyether and Schiff-base sites of each complex in each case.⁴⁰ The structural data for each complex are also summarized in Table 1, and details can be found in the Supporting Information (SI), pp S83–S120.

On the one hand, within the series of structures presented here, the value of the formal coordination number (CN) for the secondary cation in each structure appears influenced by both its ionic radius-driven bonding preferences as well as the steric requirements of the ligand. The influence of the ligand structure is especially pronounced for the smaller cations. For the structures containing monovalent secondary cations, the larger K⁺ ion adopts a CN = 7 (see SI, pp S88–S91, for details), while the smaller Li⁺ adopts CN = 6. Along this line, we note that assignment of “correct” formal coordination numbers for the secondary metal cations, and consequently their ionic radii, is challenging in work of the type reported here. The secondary cations are, after all, located in very different environments than those used to determine their ionic radii. Therefore, we note that correlations with these descriptors can be made, but only with care and attention to detail.

In the Li⁺ structure, this coordination number is achieved due to the flexibility of the polyether site; the polyether “arms” can wrap tightly around Li⁺ because of their freedom to move out of the plane defined by the rather coplanar atoms of the Schiff-base site. This tendency toward encapsulation of the monovalent cations by the polyether “arms” is also apparent in the location of the triflate counter-anions in the outer coordination spheres; the triflates appear pushed to the outer sphere since the tiara ligand system can adapt to the natural bonding preferences of the cations in each case. The two planar phenoxide-containing components of the Schiff-base site can and do fold about their O···N polyhedral edges, however, due to the saturated nature of the ethylene link between the two nitrogens; this is apparent in both the fold angles (χ) defined by those planar components as well as the O3···O6 separation that varies across the series of complexes (Figure S176).

The structures of $[\text{Ni},\text{Sr}]^{\text{T}}$ and $[\text{Ni},\text{Zn}]^{\text{T}}$ support these interpretations, with the larger Sr²⁺ ion adopting CN = 8/9 through coordination of all six oxygen atoms of the polyether site as well as two triflate counter-anions ($[\kappa^1\kappa^1]$ for CN = 8 and $[\kappa^1\kappa^2]$ for CN = 9). Smaller Zn²⁺, however, appears more encapsulated in the polyether site, with one of the ligand “arms” pulled out of the ligand plane to form a metal-binding cradle. The other ligand “arm” remains in the plane to coordinate Zn²⁺, leaving the top hemisphere open for the binding of a κ^1 -triflate, which gives a total CN = 7. The trivalent complex $[\text{Ni},\text{Lu}]^{\text{T}}$ adopts CN = 9, as the ligand “arms” wrap laterally around the sides of Lu³⁺ in the ligand plane, leaving ample space on the coordination sphere for the

binding of all three accompanying triflate counteranions in the κ^1 fashion. Only one molecule of each complex was found in the corresponding asymmetric units, except in the case of $[\text{Ni},\text{Lu}]^{\text{T}}$. However, the two molecules of $[\text{Ni},\text{Lu}]^{\text{T}}$ found in the asymmetric unit of the corresponding structure appear structurally quite similar, supporting the robustness of the conclusions drawn here (Figure S166).

On the other hand, the structural properties of the nickel center in the Schiff-base binding site do not appear strongly influenced by the secondary metal cations. The $\text{Ni}-\text{N}_{\text{imine}}$ and $\text{Ni}-\text{O}_{\text{phen}}$ distances are indistinguishable across the series (3σ criterion), and the τ^4 geometry indices remain near zero for all the complexes, suggesting that the environment of the nickel center does not change significantly upon incorporation of the secondary cations.⁴² This is attributable to the chelating and rather rigid nature of the Schiff-base site, a finding similar to that encountered in the analogous heterobimetallic complexes based on the $[\text{Ni}]^{\text{C}}$ system. This concept is supported here by the ψ_{Ni} values, which show that the nickel center remains near to the mean plane defined by the donor atoms of the Schiff-base site (O1, O2, N1, and N2). Similarly, there is virtually no out-of-plane distortion of the N_{imine} and O_{phen} atoms defining the Schiff-base site (defined as the ω_{Salmen} parameter; Table 1), confirming the flatness and covalent nature of this site across all the derivatives explored here. Considering all of these quantitative metrics, the nickel sites in the $[\text{Ni},\text{M}]^{\text{T}}$ series of complexes appear quite structurally consistent in the solid state. The similarity of the bond distances about nickel does not extend to the aforementioned polyhedral edge fold angle, which increases most significantly for $[\text{Ni},\text{Zn}]^{\text{T}}$ and $[\text{Ni},\text{Lu}]^{\text{T}}$; this is attributable to the moderately small size and high Lewis acidity of these cations.

The overall tiara ligand system developed in this work appears quite flexible and is able to cleanly bind even the smaller cations Li^+ and Zn^{2+} . This ability, in turn, has enabled exploration of charge-dependent structural parameters over a wider span of cation sizes than what was achieved in the prior work with the complexes $[\text{Ni},\text{M}]^{\text{C}}$.²² This is exemplified by the dependence of the $\text{Ni}\cdots\text{M}$ distances for the heterobimetallic complexes in the $[\text{Ni},\text{M}]^{\text{T}}$ family on the Shannon ionic radii⁴¹ of the corresponding secondary cations (Figure 3). This relationship was quantified by the slope (unitless) of the relationship, which has the value of 0.95 (± 0.01); the uncertainty on this value is only 1.1%, in accord with the good correlation displayed in the data ($R^2 = 0.99$). In the prior work with the complexes $[\text{Ni},\text{M}]^{\text{C}}$, a similar linear relationship was encountered, albeit with a more modest slope of 0.70 ± 0.03 . These linear relationships can be ascribed to the tendency of the secondary cations to nestle into the binding site defined by the phenoxide oxygen atoms (O1 and O2); we have previously ascribed this tendency in the $[\text{Ni}]^{\text{C}}$ series of complexes to anionic character on these atoms induced by phenol deprotonation upon the binding of nickel(II) to the Schiff-base site, a phenomenon that is also operative here for the $[\text{Ni}]^{\text{T}}$ series. It is sensible that this behavior is common to both $[\text{Ni}]^{\text{T}}$ and $[\text{Ni}]^{\text{C}}$ since the Schiff-base nickel sites in both complexes are structurally similar.

In line with these observations, the $\text{O}1\cdots\text{O}2$ separation displays a highly correlated but nonlinear dependence on the ionic radius of M for the complexes $[\text{Ni},\text{K}]^{\text{T}}$, $[\text{Ni},\text{Sr}]^{\text{T}}$, $[\text{Ni},\text{Zn}]^{\text{T}}$, and $[\text{Ni},\text{Lu}]^{\text{T}}$ (Figure S174). As was observed for all the complexes studied in the $[\text{Ni},\text{M}]^{\text{C}}$ series, the smaller secondary cations draw together O1 and O2 upon binding,

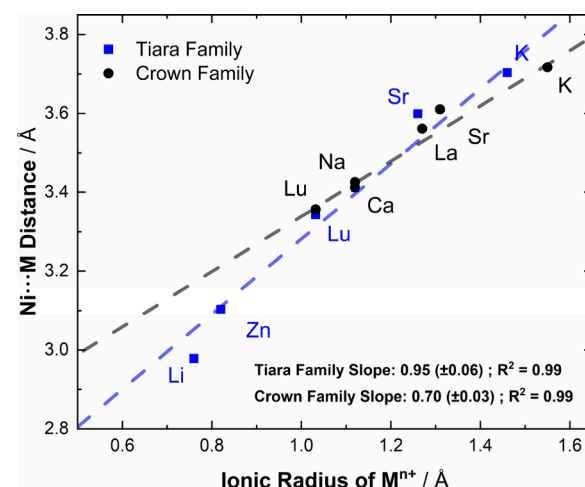


Figure 3. Trend between the Shannon ionic radius and $\text{Ni}\cdots\text{M}$ distances. Despite the similarities, there is a slight deviation of the tiara family from the crown family, resulting in a slightly higher sensitivity of the $\text{Ni}\cdots\text{M}$ distance to the Shannon ionic radius of the incorporated secondary cation (M).

tightening the diamond core motif by nestling more tightly into the site. In the case of the $[\text{Ni}]^{\text{T}}$ ligand, however, we could probe the consequences of binding even smaller cations than those used in the $[\text{Ni},\text{M}]^{\text{C}}$ series, namely, Li^+ ($r = 0.76$ Å for $\text{CN} = 6$) and Zn^{2+} ($r = 0.82$ Å for $\text{CN} = 7$; see Table 1 for details). Perhaps unsurprisingly, the $\text{O}1\cdots\text{O}2$ separation is actually smallest for $[\text{Ni},\text{Zn}]^{\text{T}}$ with a distance of $2.380(4)$ Å, much smaller than the van der Waals limit for oxygen of 2.8 Å.⁴³ This is presumably due to the high charge and small radius of zinc, as well as the unusual pentagonal-bipyramidal geometry of zinc (Figure S157).

In the case of even smaller Li^+ , the $\text{O}1\cdots\text{O}2$ distance increases to $2.442(4)$ Å; this observation is attributable to the lower charge on the lithium cation (in comparison to Zn^{2+}) as well as the non- C_2 -symmetric bicapped tetrahedral coordination of Li^+ in $[\text{Ni},\text{Li}]^{\text{T}}$ (Figures S147 and S148). This coordination environment is achieved by interaction of the cation with O1, O2, O4, and O5 in the tetrahedral polyhedron and with O3 and O6 as capping ligands on opposing faces, as highlighted in Figure S147. Li^+ is too small to interact symmetrically with both phenoxide oxygen atoms, as the $\text{Li}\cdots\text{O}1$ and $\text{Li}\cdots\text{O}2$ distances are $1.977(8)$ and $2.051(9)$ Å, respectively. As a result, the $\text{O}1\cdots\text{O}2$ separation trends longer for the adduct of Li^+ in comparison for the adduct of Zn^{2+} ; this is apparently a consequence of the very small size of this cation that causes it to slip toward one side of the pseudo- C_2 -symmetric polyether site. This tendency to slip to one side is confirmed by the observation of a $\text{Li}\cdots\text{O}6$ contact of $2.646(8)$ Å and a longer contact for $\text{Li}\cdots\text{O}3$ of $2.780(9)$ Å. Along the same line, we note that even though O3 and O6 are constrained by the tiara ligand to be positioned far apart when the Schiff base is coordinated to a metal, the $\text{O}3\cdots\text{O}6$ separation ranges from 4.613 Å for $[\text{Ni},\text{Zn}]^{\text{T}}$ to 5.353 Å for $[\text{Ni},\text{Sr}]^{\text{T}}$ (Figure S176). This range can be attributed to the tendency of the smaller and more effectively Lewis acidic cations to induce the aforementioned folding along the $\text{N}\cdots\text{O}$ polyhedral edges of the nickel site. The modest value of the fold angle for $[\text{Ni},\text{Li}]^{\text{T}}$ of 6.6° is attributable, however, to the weak interactions of Li^+ with O3 and O6 due to its small size.

In order to execute a structural comparison of the macrocyclic and nonmacrocyclic polyether sites present in the crown- and tiara- ligands, respectively, we examined the so-called ω_{tiara} parameter for each of the complexes $[\text{Ni},\text{M}]^{\text{T}}$. The ω_{tiara} parameter was calculated as the root-mean-square deviation (RMSD) of atoms O1–O6 from the average plane defined by their positions, making it a measure of the coplanarity of these atoms in the polyether site. We note here that ω_{tiara} represents the analogue of our previously described parameter ω_{crown} , as described first in ref 12; ω_{tiara} and ω_{crown} are closely related variants of what could be termed as ω_{O6} for general comparisons between cyclic and acyclic polyether sites. (ω_{O6} can therefore formally be defined formally as the RMSD of atoms O1–O6 from the average plane defined by their positions in either a “tiara” or “crown” context.) Because of the close similarity of the metalloligands $[\text{Ni}]^{\text{T}}$ and $[\text{Ni}]^{\text{C}}$, examination of this parameter affords a quantitative measure of the greater flexibility of the tiara system compared to the crown analogue. For the derivatives of both $[\text{Ni},\text{M}]^{\text{T}}$ and $[\text{Ni},\text{M}]^{\text{C}}$ for which we have structural data, the ω_{O6} parameter is systematically greater for the tiara system in all cases. For K^+ , ω_{tiara} is 0.534 and ω_{crown} is 0.107; for Sr^{2+} , ω_{tiara} is 0.124 and ω_{crown} is 0.090; and for Lu^{3+} , ω_{tiara} is 0.634 and ω_{crown} is 0.585. Consequently, the tiara ligand can be concluded to be better suited to structurally encapsulating cations in comparison with its crown analogue. The macrocyclic crown system tends to pull the donor atoms in the ring into a plane defined by its structural connectivity pattern; this is even reflected in the ω_{tiara} and ω_{crown} values of 0.245 and 0.255, respectively, for $[\text{Ni},\text{H}_2\text{O}]^{\text{T}}$ and $[\text{Ni},\text{H}_2\text{O}]^{\text{C}}$, the structures of which both feature water molecules bound in the polyether sites. Considering all this, it is sensible that adducts of the smaller cations Li^+ and Zn^{2+} could be isolated cleanly, and that they do not appear to show dynamic exchange behavior in NMR studies (*vide supra*). This capability could be useful considering the Lewis acidic properties of these cations, and the poor size match of Li^+ and Zn^{2+} with conventional 18-crown-6 systems. We note this because it represents an advantage associated with building heterometallic systems with more flexible tiara-type ligand systems rather than conventional, macrocyclic crown-type systems that have so far attracted more attention in the literature.

Electronic Absorption Spectroscopy. In the field, tunable heterobimetallic complexes assembled with a range of secondary metal cations are typically prepared in order to access chemical properties that are inaccessible for the monometallic precursors/analogs. With the ability to prepare heterobimetallics on the tiara platform now established across a wide range of metal cations, quantification of the influence of the cations on the electronic properties of the assembled complexes was next pursued. The monometallic complex $[\text{Ni}]^{\text{T}}$ exhibited a moderately intense absorption feature with wavelength of maximum absorption (λ_{max}) value of 418 nm (Figure S27); this feature was assigned as a charge-transfer (CT) transition on the basis of its moderate molar absorptivity (ϵ) of $5,800 \text{ M}^{-1} \text{ cm}^{-1}$. The assignment of this CT feature is also in accord with prior work on Schiff-base complexes featuring crown-containing macrocyclic ligands similar to the tiara present in $[\text{Ni}]^{\text{T}}$.^{23,22,44} The CT transition measured for $[\text{Ni}]^{\text{T}}$ is quite similar to an analogous transition measured for $[\text{Ni}]^{\text{C}}$ with $\lambda_{\text{max}} = 418 \text{ nm}$ and $\epsilon_{418} = 5,400 \text{ M}^{-1} \text{ cm}^{-1}$. The presence of similar transitions for $[\text{Ni}]^{\text{T}}$ and $[\text{Ni}]^{\text{C}}$ is consistent with the virtually indistinguishable structural

characteristics of the Schiff-base site in which nickel(II) is bound in both systems (see Tables S6 and S7 for details).

Similar spectral properties were measured for the $[\text{Ni},\text{M}]^{\text{T}}$ complexes in all cases. Upon installation of the secondary metal cations in the polyether site, the CT band measured for $[\text{Ni}]^{\text{T}}$ was blueshifted, as seen in Figure 4. The most significant

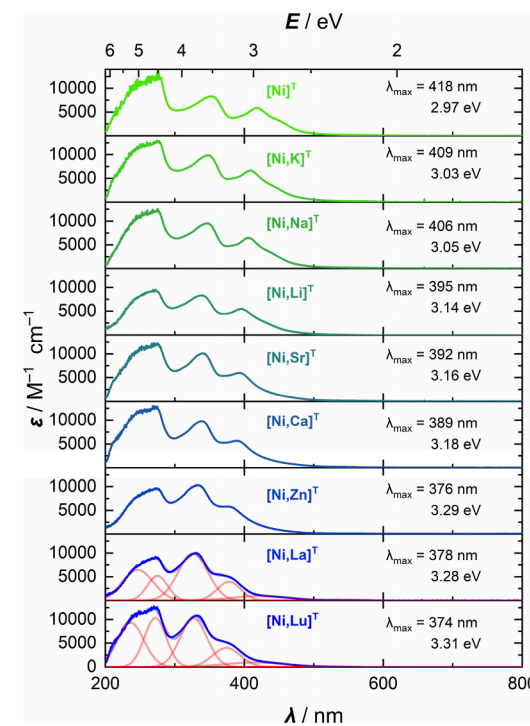


Figure 4. Electronic absorption spectra of the $[\text{Ni},\text{M}]^{\text{T}}$ complexes. The features for $[\text{Ni},\text{La}]^{\text{T}}$ and $[\text{Ni},\text{Lu}]^{\text{T}}$ given in the red lines were fit using Gaussian peak deconvolution in order to obtain a reliable value for the lowest-energy CT transition as discussed in the main text. In each case, the $[\text{Ni}]$ was 0.2 mM and the path length of the cuvette used for the measurements was 1 cm.

shift, to $\lambda_{\text{max}} = 374 \text{ nm}$, was measured for the most Lewis acidic metal cation, Lu^{3+} . As was measured previously for the $[\text{Ni},\text{M}]^{\text{C}}$ series, the most charge-dense secondary metal cations induce the most significant spectral changes.^{12,22,23,44} Plotting the energy of the CT transition as a function of the $\text{p}K_a$ value of the corresponding secondary metal cation revealed a linear dependence as seen in Figure 5, in line with reports regarding the optical properties of other systems based on Reinhoudt-type ligands. The slope of the dependence of the energy of the CT transition on the cation $\text{p}K_a$ value is $-35 \pm 2 \text{ meV per } \text{p}K_a$; this value is statistically indistinguishable from the value reported for the $[\text{Ni},\text{M}]^{\text{C}}$ series, $-36 \pm 5 \text{ meV per } \text{p}K_a$, within the uncertainty associated with the correlation (quoted at the 1σ level in both cases). These virtually identical findings across the two ligand systems indicate that electronic properties of the two resulting classes of complexes are quite similar.

In prior work on the $[\text{Ni},\text{M}]^{\text{C}}$ complexes, d-d transitions were measured between 545 and 532 nm. Corresponding d-d transitions could not be measured in the cases of the $[\text{Ni},\text{M}]^{\text{T}}$ complexes, however, a finding attributable to greater broadness of the CT features in the spectra for the nonmacrocyclic complexes (Figure S47). At this stage, we anticipate that the greater broadness of the absorption features encountered with these complexes is attributable to a greater degree of structural

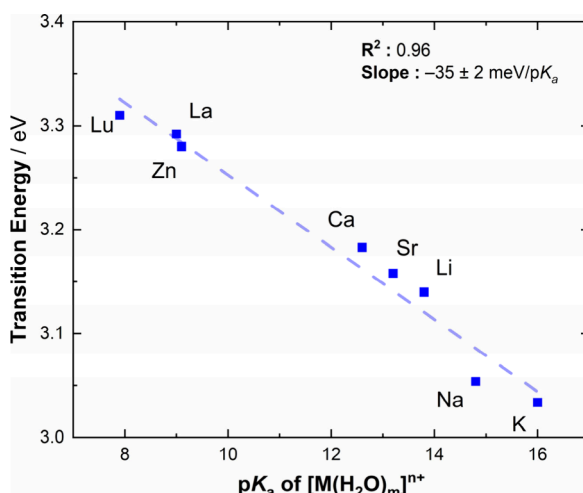


Figure 5. Plot showing the dependence of the CT transition energies on the pK_a values of the metal aqua complexes corresponding to the cations incorporated into the $[\text{Ni},\text{M}]^{\text{T}}$ complexes.

flexibility, as engendered by the tiara ligand system; the “arms” of the tiara polyether moiety can adopt more structurally diverse conformations than the crown-type polyether motif, as shown in the structural data. We anticipate that this is also true in solution, in that the tiara-type polyether moieties in the $[\text{Ni},\text{M}]^{\text{T}}$ complexes could be more flexible and dynamic. Although d-d transitions could not be conclusively identified for most of the $[\text{Ni},\text{M}]^{\text{T}}$ complexes, it was possible to observe shoulder features on the lowest energy CT transitions around 560 nm in the case of $[\text{Ni}]^{\text{T}}$ and around 540 nm in the case of $[\text{Ni},\text{Lu}]^{\text{T}}$. As the d-d transitions in the $[\text{Ni},\text{M}]^{\text{C}}$ complexes spanned a range of λ_{max} of 550 to 532 nm, the noted shoulders measured for the tiara-type systems are likely attributable to d-d transitions. The observation of possible d-d transitions for the $[\text{Ni},\text{M}]^{\text{T}}$ complexes is in accord with the general conclusion that the electronic properties of the tiara complexes are quite similar to their crown analogues.

Titration Studies of Cation Binding to the Tiara and Crown Systems. In order to further investigate the similarities and possible differences between the tiara and crown ligand systems, we carried out titration studies of cation binding with UV-visible spectroscopic monitoring. In this work, solutions containing either 0.1 mM $[\text{Ni}]^{\text{T}}$ or 0.1 mM $[\text{Ni}]^{\text{C}}$ were titrated with a standard series of triflate salts (KOTf, LiOTf, Sr(OTf)₂, or Lu(OTf)₃) in order to ascertain if binding of the cations to the parent nickel complexes was tight and if the spectral data for the heterobimetallic species formed *in situ* would compare well to those corresponding to the as-synthesized/isolated 1:1 $[\text{Ni},\text{M}]^{\text{T}}$ complexes. Comparison of these spectral data and the overall profile of each titration affords insight into whether the cation present in each complex tends to be fully bound in solution or if it does not, instead being involved in an equilibrium between bound and free species. Additionally, titrations of solutions of $[\text{Ni}]^{\text{T}}$ and $[\text{Ni}]^{\text{C}}$ were conducted with CsOTf, in order to ascertain if the closed (crown) or open (tiara) chain system would bind a larger ion like Cs⁺ more effectively (Cs⁺ with CN = 8 has $r = 1.74 \text{ \AA}$).⁴¹ Data for the titration of $[\text{Ni}]^{\text{T}}$ with Sr(OTf)₂ are shown in Figure 6, and the data for all of the titrations carried out in the course of this work are given in the SI, pp S32–S56.

The data corresponding to titration of $[\text{Ni}]^{\text{T}}$ and $[\text{Ni}]^{\text{C}}$ with KOTf indicate tight binding of K⁺ to the polyether moieties

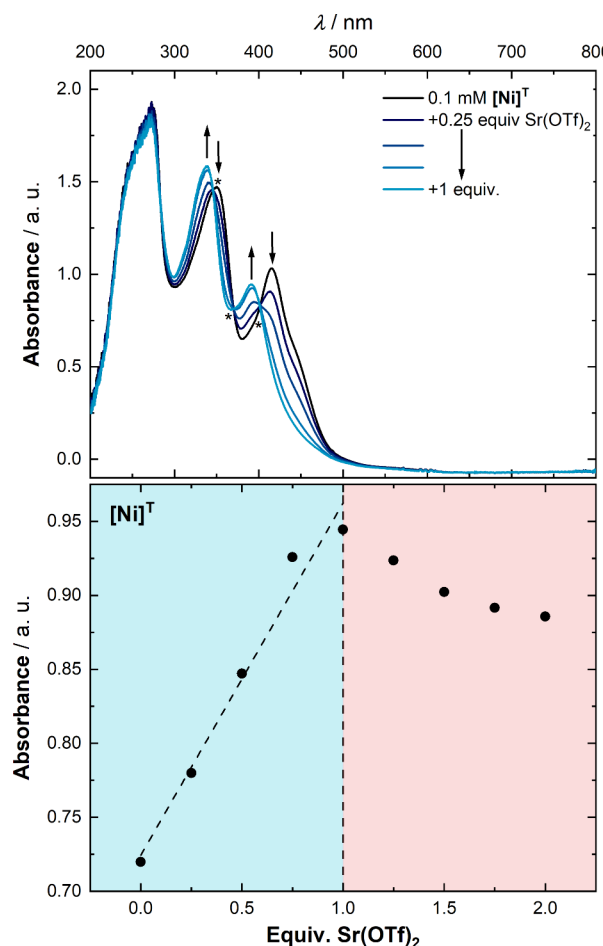


Figure 6. Spectral data and analysis for the titration of a 0.1-mM solution of $[\text{Ni}]^{\text{T}}$ with Sr(OTf)₂ in CH_3CN . Upper panel: electronic absorption spectra for individual steps in the titration up to addition of one equivalent Sr(OTf)₂. Isosbestic points are indicated with asterisks (*) and are located at 346, 370, and 401 nm. Lower panel: plot of the absorbance measured at 392 nm vs the added equivalents of Sr(OTf)₂ in solution. 392 nm corresponds to the λ_{max} value of the lowest-energy CT transition for the heterobimetallic species in solution. The linear increase in absorbance up to addition of one equivalent of Sr(OTf)₂, the lack of additional increases in absorbance beyond addition of one equivalent of Sr(OTf)₂, and the apparent dilution behavior that occurs at higher additions are all consistent with tight binding of one equivalent of Sr²⁺ to $[\text{Ni}]^{\text{T}}$ in this system. For the linear fit of the increasing absorbance data up to one equivalent, $R^2 = 0.975$.

present in both monometallic complexes (Figures S48–S54). Very similar isosbestic spectral changes were measured up to addition of 1 equiv of KOTf in both titrations; isosbestic points were measured at 376 and 408 nm in the case of $[\text{Ni}]^{\text{T}}$ and at 376 and 410 nm in the case of $[\text{Ni}]^{\text{C}}$. A distinct lack of curvature in the absorbance at λ_{max} vs $[\text{K}^+]$ data for both systems is indicative of tight binding of K⁺ under these conditions (Figure S50 and S53). This means that up to 1 equiv of K⁺ is tightly bound by either system; little K⁺ is implied to be free in solution under these conditions. Addition of >1 equiv of KOTf results only in dilution behavior (diminished absorption across the full spectral range), as shown by the data corresponding to higher cation equivalencies. Comparison of the spectral data (e.g., apparent λ_{max} values) obtained in the titration for the 1:1 mixture of

$[\text{Ni}]^T$ and KOTf compares well with the electronic absorption data collected for as-synthesized $[\text{Ni},\text{K}]^T$ as well (Table S1). Considering all this evidence, as well as the similar spectral profiles for the titrated samples of $[\text{Ni},\text{K}]^T$ and $[\text{Ni},\text{K}]^C$ (Figure S54), the behavior of $[\text{Ni}]^T$ and $[\text{Ni}]^C$ with KOTf can be concluded to be quite similar and well in line with the similar structures from XRD analysis for the characterized adducts.

Similar results were obtained for the titrations of $[\text{Ni}]^T$ and $[\text{Ni}]^C$ with LiOTf and $\text{Sr}(\text{OTf})_2$ (Figures S55–S68). Titration of each monometallic nickel complex with up to 1 equiv of either salt showed isosbestic behavior and spectral changes consistent with *in situ* formation of the desired 1:1 heterobimetallic species. Plotting the absorbance at the λ_{max} value corresponding to the lowest-energy CT transition in each case reveals similar behavior, indicative of tight binding of up to 1 equiv of Li^+ or Sr^{2+} in both the tiara polyether and the crown polyether sites (see Figure S60 for Li^+ data and Figure 6 for Sr^{2+} data). Distinctive dilution-only behavior was not observed following additions of LiOTf beyond 1 equiv, however, suggesting that higher-order adducts of Li^+ with the nickel complexes could be accessible in both cases. (Here, dilution behavior can be defined as a decrease in absorbance across the spectral profile upon addition of the titrant solution; all of the triflate salts used here are colorless and lack absorption features in the visible range, meaning that if no binding occurs to the nickel complex then all that is measured is a decrease in absorption for the parent metal complex.) Particular to titration of $[\text{Ni}]^T$ with $\text{Sr}(\text{OTf})_2$, the formation of only the 1:1 complex was implied by the data, given isosbestic behavior up to 1 equiv of Sr^{2+} added and dilution-only behavior upon additions of Sr^{2+} beyond 1 equiv. A similar 1:1 binding behavior was observed with the $[\text{Ni}]^C$ system as well, although minor enhancement in absorption at additions of Sr^{2+} beyond 1 equiv were also measured (Figure S67), perhaps consistent with weak simultaneous binding of cations to both faces of the cyclic crown polyether moiety.

The titrations of $[\text{Ni}]^T$ and $[\text{Ni}]^C$ with $\text{Lu}(\text{OTf})_3$ were generally well behaved as well. On the one hand, λ_{max} values similar to those measured for as-synthesized $[\text{Ni},\text{Lu}]^T$ and $[\text{Ni},\text{Lu}]^C$ were obtained when 1 equiv of $\text{Lu}(\text{OTf})_3$ was added to either monometallic complex (Table S1). Additionally, little curvature is observable in plots of absorbance vs $[\text{Lu}^{3+}]$ from these experiments, suggestive of tight binding of the cations in the polyether sites (Figures S71 and S74). However, the titrations of both systems with Lu^{3+} were not as monotonic up to addition of one equivalent as those for the other cations. In the case of $[\text{Ni}]^T$, virtually linear changes in absorbance were obtained upon titration with up to 0.75 equiv of Lu^{3+} , and then little change was measured for equivalencies >0.75 (Figure S71). Similarly, in the case of $[\text{Ni}]^C$, virtually linear changes in absorbance were obtained upon titration with up to 1.25 equiv of Lu^{3+} , and then little change was measured upon addition of further cation (Figure S74). In the cases of both nickel complexes, however, the spectral changes up to addition of one equivalent of Lu^{3+} were virtually isosbestic in both cases (Figures S69 and S72). As the $\text{Lu}(\text{OTf})_3$ used in the course of this work was characterized prior to use by infrared and ^{19}F NMR spectroscopy, found to be anhydrous by methods previously described by our group,⁴⁵ and stored/handled only in an inert-atmosphere glovebox for these studies, we anticipate that the stated composition of the salt was reliable at the time of these experiments. Consequently, we conclude

that this trivalent cation may induce additional (minor) speciation along the path to the 1:1 $\text{Ni}:\text{Lu}$ adduct, especially for the tiara system. This may be consistent with the observation of two closely related but nonetheless structurally distinct isomers of $[\text{Ni},\text{Lu}]^T$ in the solid-state data for this complex (see the SI, pp S106–S114). It may also be consistent with the tendency for trivalent cations to bind more tightly to ligands, like the oxygen atoms of the polyether group, than their mono- and divalent analogues.^{45,46}

Titration of $[\text{Ni}]^T$ with CsOTf resulted in only minor spectral changes (Figures S76–S79). In particular, plotting the absorbance around $\lambda_{\text{max}} = 415\text{--}410\text{ nm}$ vs $[\text{Cs}^+]$ revealed a diminished absorbance across the full range, with somewhat linear decreases at up to 0.5 equiv added (Figure S79). We note that the λ_{max} value corresponding to the lowest-energy CT transition shifted over the course of the experiment (Figure S78), suggesting exchange phenomena impact this system; this observation is consistent with the modest Lewis acidity and modest tendency to bind ligands that has been established for Cs^+ .⁴⁶ Further additions beyond one equivalent of Cs^+ caused diminishment in absorbance as well (Figure S79). Examining the value of λ_{max} near 415 nm over the full titration range revealed only a 4 nm shift in λ_{max} ; this finding is consistent with only a minor influence of Cs^+ on the spectral properties of $[\text{Ni}]^T$ and could be consistent with limited interaction as well. Consequently, we conclude that $[\text{Ni}]^T$ interacts weakly with Cs^+ , although the formation of a 2:1 adduct is possible based on the unique data profile up to addition of one equivalent of CsOTf . Titration of $[\text{Ni}]^C$ with CsOTf , however, revealed a clear binding of Cs^+ to the monometallic precursor; one regime of clear spectral changes were measured up to addition of 0.5 equiv, and then a second regime of spectral changes were observed out to 2.0 equiv (Figures S80–S83). These data are consistent with much stronger formation of a 2:1 adduct of the crown system with Cs^+ ; the species formed in this case would likely adopt a “sandwich” configuration in which the large cesium cation is held between the two 18-crown-6-like moieties of $[\text{Ni}]^C$. In such a structure, the triflate counter-anions would likely be located in the outer coordination sphere. And, we note here, that the lower degrees of freedom in the crown system likely engender the more significant/stable formation of the 2:1 adduct; the macrocyclic nature of the crown system should drive a tendency for greater planarity. Planarity of this type would facilitate the formation of “sandwich” configurations with larger cations like Cs^+ . Initially, we considered the possibility that the tiara would bind Cs^+ more readily due to its flexibility, but this does not appear to be the case based on the titration data from this study.

Considering all these titration results, the tiara system can be concluded to be as effective or even superior in performance toward the binding of most cations, including K^+ , Li^+ , and Sr^{2+} . This conclusion is based on the similar, isosbestic, and clean titration behaviors with these cations for both $[\text{Ni}]^T$ and $[\text{Ni}]^C$. One equivalent of each cation is cleanly and tightly bound by each system, confirming that the macrocyclic connectivity of $[\text{Ni}]^C$ is not required to obtain complete binding of one cation in acetonitrile. Similar results for Lu^{3+} were found with $[\text{Ni}]^T$ and $[\text{Ni}]^C$, and we note that the 1:1 adducts of each system with Lu^{3+} could be cleanly isolated at synthetic scale in each case. Nonetheless, the absorbance vs $[\text{Lu}^{3+}]$ are more complex than in the cases of the other cations, perhaps suggestive of speciation that is strongly dependent upon $[\text{Lu}^{3+}]$. And finally, CsOTf appears to interact only weakly with $[\text{Ni}]^T$, suggesting

that the tiara motif is less suited to tight binding of large cations with modest charges. A 2:1 Cs:Ni adduct can apparently be formed with the crown system $[\text{Ni}]^{\text{C}}$, however, in line with prior findings on “sandwich” structures in which Cs^+ has been found to interact simultaneously with two 18-crown-6 moieties.⁴⁷ The planarity of $[\text{Ni}]^{\text{C}}$ that is enforced by its macrocyclic nature would appear to give some advantage toward the formation of such structures in the crown case explored here.

Electrochemical Studies. Given the similarity in the electronic spectra for the $[\text{Ni},\text{M}]^{\text{T}}$ and $[\text{Ni},\text{M}]^{\text{C}}$ complexes, the electrochemical properties of the complexes were anticipated to be similar for the two families as well. Although in the case of the $[\text{Ni},\text{M}]^{\text{T}}$ complexes, one might hypothesize that there could be a greater propensity toward electrochemically induced reactivity considering the lack of macrocyclic stabilization of the complexes in comparison to prior crown-based systems, we have not found the $[\text{Ni},\text{M}]^{\text{T}}$ complexes to display problematic or suboptimal electrochemical properties indicative of redox induced reactivity/speciation, except in the case of $[\text{Ni},\text{Zn}]^{\text{T}}$.

Analysis of the electrochemical properties of the non-macrocyclic complexes studied here began with the monometallic precursor complex $[\text{Ni}]^{\text{T}}$ and interrogation of the electrochemistry at negative potentials (Figures S57–S66). Cyclic voltammetry (CV) data collected for $[\text{Ni}]^{\text{T}}$ exhibited a quasi-reversible reduction at $E_{1/2} = -2.10$ V vs the ferrocenium/ferrocene couple (hereafter referred to as $\text{Fc}^{+/-}$) as shown in Figure 7. The measured couple retained its quasi-

$= 40$ mV). The peak-to-peak separations (ΔE_p values) for both $[\text{Ni}]^{\text{T}}$ and $[\text{Ni}]^{\text{C}}$ were 84 and 75 mV when measured at 100 mV/s (Table 2), indicating reasonably fast ET for our experimental configuration in both cases.⁴⁸ Based on the profiles of the voltammetry data, both $[\text{Ni}]^{\text{T}}$ and $[\text{Ni}]^{\text{C}}$ display well-behaved, chemically reversible reduction waves.

For the heterobimetallic complexes in the $[\text{Ni},\text{M}]^{\text{T}}$ family, electrochemical reduction waves were measured in each case that appeared quasi-reversible at 100 mV/s (Figure 7 and Table 2). The incorporation of secondary metal cations resulted in shifts in the reduction potentials of the complexes to more positive voltages in all cases. Each individual redox couple was interrogated with scan-rate dependent studies, and both the oxidized and reduced forms of each species were shown to be freely diffusional and soluble in each case (see the SI, pp S57–S66). The cyclic voltammetric profile of $[\text{Ni},\text{Zn}]^{\text{T}}$ was the only one to deviate from conventional behaviors; in this case, the complex displayed a rather broad cathodic peak compared to the other complexes in this study, as shown in Figure S97. A minor reaction channel involving reduction-induced speciation could be involved in this system, as voltammograms collected at slower scan rates displayed a greater deviation from conventional wave shape and a minor shoulder feature on the low potential side of the anodic return wave. When the switching potential was set to less negative potentials, the additional oxidative feature was minimized, suggesting the involvement of reduction-induced reactivity (Figure S98). However, this complication did not impede the electrochemical work with $[\text{Ni},\text{Zn}]^{\text{T}}$, enabling us to examine this complex similar to all the other derivatives prepared here.

For the complexes of the $[\text{Ni},\text{M}]^{\text{T}}$ family, the more positive potentials are associated with the derivatives incorporating metal cations that feature greater effective Lewis acidity, as judged by the $\text{p}K_a$ values of the corresponding metal aqua complexes. This result is similar to that encountered in the $[\text{Ni},\text{M}]^{\text{C}}$ family of complexes, in which the reduction potential appeared to depend on the charge of the secondary metal cations; the cations with greater positive charges resulted in more positive reduction potentials.^{2,4,22} However, in the present study, the use of the tiara ligand system enabled us to explore a wider range of metal cations that span a greater range of Lewis acidity values than in the studies of the $[\text{Ni},\text{M}]^{\text{C}}$ family, particularly among the monovalent and divalent cations. Among monovalents, $[\text{Ni},\text{K}]^{\text{T}}$ and $[\text{Ni},\text{Li}]^{\text{T}}$ were prepared, representing a span of corresponding $\text{p}K_a$ values from 16.0 to 13.8, respectively. Among divalents, $[\text{Ni},\text{Sr}]^{\text{T}}$ and $[\text{Ni},\text{Zn}]^{\text{T}}$ were prepared, representing a span of $\text{p}K_a$ values from 13.2 to 9.0, respectively. As a result, the most acidic monovalent cation (Li^+) is nearly as acidic as the least acidic divalent cation (Sr^{2+}). Similarly, the most acidic divalent cation (Zn^{2+}) is more acidic than the least acidic trivalent cation used in this study (La^{3+} , $\text{p}K_a = 9.1$). As a result of the exploration of this diverse set of cations, the relationship between reduction potential and Lewis acidity could be examined across sufficiently diverse cations that the cations are not clustered according to valence in the data, but rather widely spaced in the broader chemical space of cation-dependent acidity (Figure 8).

The data given in Figure 8 shows that the reduction potential for the heterobimetallic complexes does not depend linearly on charge as has been found in some prior studies. We hypothesize that findings of charge-dependent redox properties may be attributable to the collection of data on insufficiently

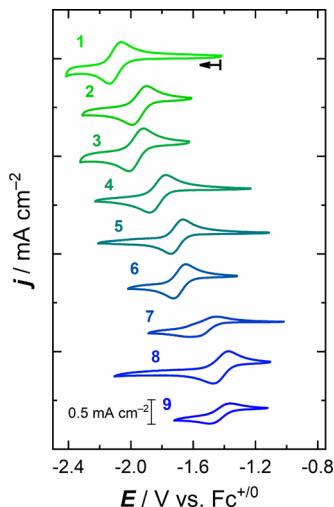


Figure 7. Plot showing the cyclic voltammograms corresponding to data collected at negative potentials for $[\text{Ni}]^{\text{T}}$ and the heterobimetallic complexes in the $[\text{Ni},\text{M}]^{\text{T}}$ family. All voltammograms were collected at a scan rate of 100 mV/s with $[\text{Ni}] = 2$ mM in acetonitrile containing 0.1 M tetrabutylammonium hexafluorophosphate as supporting electrolyte.

reversible nature across the range of scan rates used in this study (50–1000 mV/s; Figure S49). These data also confirmed the freely diffusional and soluble nature of both the oxidized, Ni(II), and reduced, putative Ni(I), forms of the complex in solution, as well as high stability of the reduced species on the time scale of the CV experiments. The reduction potential measured for $[\text{Ni}]^{\text{C}}$ was $E_{1/2} = -2.14$ V vs $\text{Fc}^{+/-}$, in accord with very similar redox properties in both cases ($\Delta E_{1/2}$

Table 2. Comparison of Electrochemical Parameters Obtained via Cyclic Voltammetry

compound	M	pK_a of $[M(H_2O)_n]^{n+}$ ^a	$E_{1/2}$ (V)	$\Delta E_{1/2}$ vs $[Ni]$ (mV) ^b	ΔE_p (mV) ^b	k^0 ($cm/s \times 10^3$) ^d	% V_f^e
$[Ni]^T$			-2.10	0	75	11.6 ± 0.7	45.8 ^c
$[Ni,K]^T$	K	16	-1.94	157	96	4.2 ± 0.3	37.2
$[Ni,Na]^T$	Na	14.7	-1.91	182	93	4.4 ± 0.4	
$[Ni,Li]^T$	Li	13.8	-1.83	274	105	2.8 ± 0.3	39.8
$[Ni,Sr]^T$	Sr	13.2	-1.70	396	76	10.6 ± 0.5	33.8 ^c
$[Ni,Ca]^T$	Ca	12.7	-1.69	414	78	9.7 ± 0.4	
$[Ni,Zn]^T$	Zn	9.0	-1.54	565	170		32.1
$[Ni,La]^T$	La	9.1	-1.42	680	99	4.5 ± 0.3	
$[Ni,Lu]^T$	Lu	7.9	-1.43	673	130	2.3 ± 0.1	23.4 ^c

^aFrom ref 39. ^bMeasured at 100 mV/s. ^cValues obtained as an average of multiple molecules in the solid-state structure. The span between the two values that were averaged are as follows: 0.2% for $[Ni, H_2O]^T$; 0.6% for $[Ni, Sr]^T$; 0.8% for $[Ni, Lu]^T$. ^dFor the chemically reversible redox cycling at negative potentials. The reported value is the arithmetic mean of the individual rates that were determined at five different scan rates (50, 100, 150, 200, and 250 mV/s). Uncertainty (reported as $\pm 1\sigma$) was calculated from the replicate data. ^eDefined as the percent free volume about the nickel center.

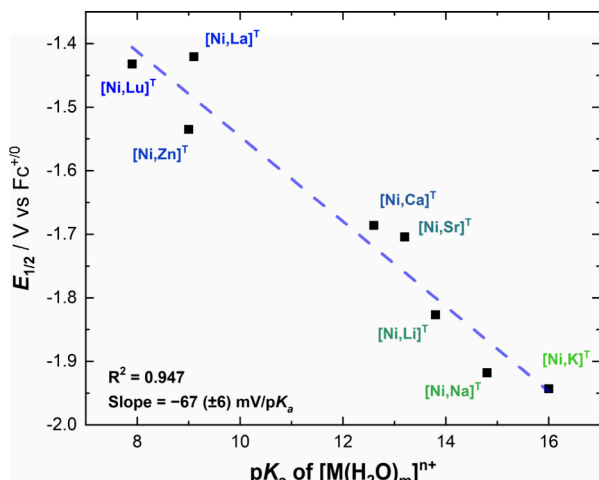


Figure 8. Plot of the formal $Ni^{II/I}$ couple of the $[Ni, M]^T$ family vs the pK_a of the relevant M aqua complexes.

diverse complexes. Additionally, we note, as we did in a recent prior study, that it is difficult (or even impossible) to rigorously ascribe a change in a reduction potential when both the oxidized and reduced forms of the complexes in question have not been characterized.²² At this stage, we can only speculate about the origins of charge- vs acidity-dependent data, but we anticipate, however, that charge-dependent behaviors may be displayed by systems in which cations can readily shift upon ET to new preferred positions; systems that can more effectively encapsulate cations, restricting their movement to some degree before/after reduction, could enable acidity-dependent behaviors to appear more clearly in electrochemical data. Regardless, we anticipate that the tiara complexes explored here represent a useful family of compounds upon which to base explorations of the redox chemistry of heterobimetallic complexes, because the tiara motif is capable of binding a wide range of metal cations.

The reduction potentials of complexes in the $[Ni, M]^T$ family display a dependence of -67 ± 6 mV/ pK_a unit when examined in this way. The modest variance on the slope of the correlation, corresponding to $\pm 9\%$ and reported as $\pm 1\sigma$, was calculated in this case from the standard error on the least-squares linear fitting to the data. This low value is in accord with the good estimated fit of each $E_{1/2}$ value to the trend ($R^2 = 0.947$). In the crown-based analogues of the $[Ni, M]^C$ family,

the slope displayed by the related data was -69 ± 7 mV/ pK_a unit, a value that is within one standard deviation of the value measured here.²² The indistinguishable slopes of these plots indicates that the influence wrought by the secondary metal cations on the redox-active nickel cores of each family of complexes are similar in each case. This is sensible given the similar structures of the heterobimetallic complexes, a finding exemplified by the data given in Figure 3. The cations in the complexes are located at very similar positions relative to the redox-active nickel center in each case. Of course, the tiara ligand is capable of greater encapsulation of the secondary cations than the crown ligand, but this appears to be a minor difference from the perspective of the redox chemistry. In both cases, the cations bind adjacent to the nickel site and from this vantage point are able to systematically shift the reduction potential on the basis of their effective Lewis acidities. Additionally, it should be noted explicitly that similar tuning effectiveness can be achieved in the tiara complexes compared to the crown complexes; the tiara complexes are simpler to prepare than their crown analogues but appear equally as useful for applications in study of cation-induced tuning. Along this line, the tiara ligand system may be concluded to be superior given its demonstrated ability to bind a wide range of cations, both in terms of Lewis acidity and in terms of size (Table 1).

Following the suggestion of one reviewer of this paper, we also interrogated the electrochemistry of the $[Ni]^T$ and the $[Ni, M]^T$ complexes at positive potentials (Figures S104–S133). This was pursued in order to determine if each of the complexes could support oxidation from the formal nickel(II) oxidation state to species that could be assigned as having the formal nickel(III) oxidation state, as well as any effect that the incorporated secondary cations might have on the potentials measured for the relevant anodic processes. Indeed, we have found that $[Ni]^T$ and the $[Ni, M]^T$ complexes can support oxidation, and that the potential for the key oxidative waves is dependent upon the identity of the incorporated secondary cations. However, we note that in the case of the Lu^{3+} adduct, the wave appears to be shifted beyond the working range of our solvent/electrolyte system; nonetheless, based on comparison to the other adducts studied here, it should be present just beyond our interrogation window. The observation of this redox at positive potentials for the $[Ni, M]^T$ series of complexes is notable, because to the best of our knowledge, no series of cation-tuned redox-active complexes has previously been

studied that can support multiple redox processes. Many have been studied that support a single redox manifold, but none that feature two (or more) sets of redox processes. Here, the opportunity thus arose to quantify how incorporated cations exert an influence over two different redox events in one family of homologous and heterobimetallic molecules.

The key cyclic voltammetric data corresponding to the interrogation of the anodic process for each nickel tiara complex is shown in Figure 9. In each case, a seemingly well-

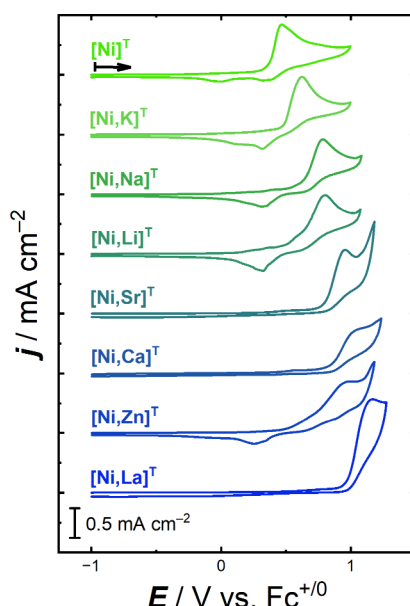


Figure 9. Plot showing cyclic voltammograms corresponding to data collected at positive potentials for $[\text{Ni}]^{\text{T}}$ and the heterobimetallic complexes in the $[\text{Ni},\text{M}]^{\text{T}}$ family. All voltammograms were collected at a scan rate of 100 mV/s with $[\text{Ni}] = 2 \text{ mM}$ in acetonitrile containing 0.1 M tetrabutylammonium hexafluorophosphate as the supporting electrolyte.

behaved anodic wave was measured around +0.5 V vs $\text{Fc}^{+}/0$. Unlike the nickel(II)/nickel(I) redox manifolds measured at negative potentials, however, the anodic waves for each complex appear chemically irreversible and thus associated with EC-type, follow-up chemical reactivity.⁴⁹ This follow-up reactivity in each case results in significant changes to the cyclic voltammetric profile upon multiple cycling, precluding some of the conventional analyses that we routinely implement when analyzing electrochemical data. In this case, it appears that new electroactive species are generated following oxidation of the starting $[\text{Ni},\text{M}]^{\text{T}}$ complexes and that these may be associated with the electrode surface. In the SI, pp S67–S82, we have included a full battery of figures that catalogue these behaviors; however, we do not discuss them further here as the as-yet undefined nature of the electroactive/electrogenerated products makes them less relevant to our goal of interrogating cation-dependent redox chemistry.

Returning to the question of the tunable molecular electrochemistry of the $[\text{Ni},\text{M}]^{\text{T}}$ complexes, it is apparent from the first scans of each voltammogram (given in Figure 9) that the synthesized molecules can undergo oxidation at the electrode surface. In each case, there is an irreversible oxidation process (associated with a peak anodic potential, denoted $E_{\text{p},\text{a}}$) corresponding to oxidation of the complex to a new species in solution. The observation of these waves is consistent with

some prior measurements that have been carried out on nickel-salen-type complexes, although we are not aware of any system in which the cation tunability of such redox has been studied in a comprehensive fashion.⁵⁰ As shown in Figure 9, incorporation of more strongly Lewis acidic cations appears to result in more positive $E_{\text{p},\text{a}}$ values in each case. For example, incorporation of K^+ results in an $E_{\text{p},\text{a}}$ value of +0.62 V, shifted positive by 150 mV when compared to the value of $E_{\text{p},\text{a}}$ for the monometallic tiara complex of +0.47 V. Similar behavior was generally observed across the series of heterobimetallic species; for example, $[\text{Ni},\text{La}]^{\text{T}}$ was found to undergo oxidation with $E_{\text{p},\text{a}}$ at +1.2 V, a shift of over 700 mV when compared to the $[\text{Ni}]^{\text{T}}$ complex. Consequently, we conclude that the oxidative processes measured at positive potentials are tuned by incorporation of secondary cations, much like the reductive processes measured at negative potentials. This result agrees with the titration studies as well, since these confirmed the stable binding of all the relevant cations explored in the electrochemical work (*vide supra*).

Considering these findings, we next moved to quantify the influence of the secondary cations on the anodic process associated with the measured $E_{\text{p},\text{a}}$ values described above. To do this, we plotted the $E_{\text{p},\text{a}}$ values as a function of the pK_a values of the incorporated secondary cations, mirroring the approach taken with the data at negative potentials shown in Figure 8. The resulting plot (Figure 10) confirms a reasonable

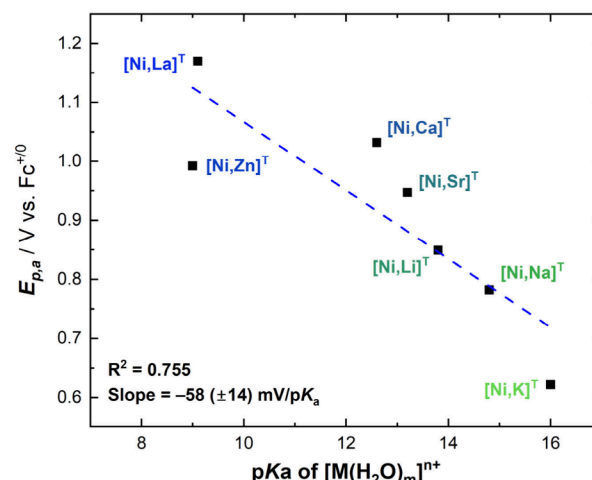


Figure 10. Plot of the oxidative $E_{\text{p},\text{a}}$ of the $[\text{Ni},\text{M}]^{\text{T}}$ family vs the pK_a of the relevant M aqua complexes.

correlation between the peak anodic potential measured for each heterobimetallic complex and the Lewis acidity of the incorporated secondary cation. Taking all of the data into consideration, the slope of the measured relationship was found to be $-58 \pm 14 \text{ mV per } \text{pK}_a$ unit, a finding that compares well with the relationship measured in the reductive data of $-67 \pm 6 \text{ mV/pK}_a$. We note, however, that the more modest potential dependence measured for the anodic redox process at positive potentials could be consistent with contribution of ligand-centered oxidation to the process. This is because we have previously found, in comparison of homologous $[\text{Ni},\text{M}]$ and $[\text{Pd},\text{M}]$ complexes built on the crown ligand system discussed here, that a purely ligand-centered reduction process for the $[\text{Pd},\text{M}]$ system displayed a more modest dependence on Lewis acidity (-48 mV/pK_a) than an analogous metal-centered $\text{Ni}^{\text{II}}/\text{Ni}^{\text{I}}$ redox manifold for the

$[\text{Ni},\text{M}]$ system (-69 mV/p K_a).^{22,23} Considering the complexes under consideration in that case were homologous, we have hypothesized that the more significant dependence of the metal-centered redox on Lewis acidity was attributable to the closer spacing of the secondary cation with the nickel center, in comparison with the redox-active conjugated system in the palladium complexes. This hypothesis appears applicable to the present oxidative electrochemistry of the $[\text{Ni},\text{M}]^T$ family of complexes, considering the spacing between the secondary Lewis acidic cations and the reductively redox-active nickel center is closer than the spacing to the conjugated ligand backbone regions that could be involved in the measured oxidative redox based on the available XRD data. Consequently, we anticipate that the measured relationship between Lewis acidity at the peak anodic potentials suggests a mixture of metal- and ligand-centered character for the oxidized species, a conclusion in accord with the relatively positive potentials involved and the established propensity of related oxidized salen-type species to be reactive.²⁰ Prior work suggests that ligand-centered oxidation would contribute significantly in this system as well.^{50b,50c}

Examining the trendline for the oxidative potentials in this study suggests there could be some factors that complicate the analysis, however. The irreversible nature of the anodic processes used to prepare the plot given in Figure 10 is among these factors, in that the peak potentials themselves could be subject to electrochemical irreversibility effects⁴⁹ that would result in the measured potentials not corresponding to pure thermodynamic influences of the secondary cations on the redox chemistry; modulation of the ET kinetics would introduce shifts into the peak-potential data. Additionally, we note that the $E_{p,a}$ value for $[\text{Ni},\text{Zn}]^T$ is not as positive in potential as one might expect in comparison to its analogues $[\text{Ni},\text{Sr}]^T$ and $[\text{Ni},\text{Ca}]^T$; we anticipate that this could be due to additional chemical reactivity/speciation behavior as was implied in the reductive electrochemistry associated with the nickel(II)/nickel(I) redox manifold. Finally, we note that the peak anodic potential measured for $[\text{Ni},\text{La}]^T$ is quite close (Figure 8 and Figure S132) to the limit at which our solvent/electrolyte appears to break down; as a result, background currents could artificially shift the measured potential. Consequently, for completeness, we have also supplied a trend plot in Figure S133 that excludes the possibly problematic points for $[\text{Ni},\text{Zn}]^T$ and $[\text{Ni},\text{La}]^T$; however, the relationship (although rather linear) between peak potential and p K_a in that plot appears far too large in absolute magnitude based on our experience in the field to be reasonable. Therefore, we anticipate that the trendline and relationship described by the full available data set given in Figure 10 represents the best choice for quantifying the electrostatic influence of the secondary cations on the anodic redox of the $[\text{Ni},\text{M}]^T$ complexes in this study. And we reiterate that completing this analysis at positive potentials complements the results from the analysis at negative potentials. Incorporated second cations can be safely concluded to be reliable modulators of reduction potentials, at least when they are bound stably by the parent redox-active frameworks.

Topographical Analysis of the Schiff-Base Sites and Analysis of the Heterogeneous ET Rates. One important finding of the previous study of the crown-based $[\text{Ni},\text{M}]^C$ family of complexes was attenuation of the heterogeneous ET rate constant (hereafter referred to as k^0) in cases in which trivalent secondary metal cations were utilized.²² This

phenomenon was found to be correlated with structural data, in that the triflate counteranions bound to the redox-inactive trivalent cations La^{3+} and Lu^{3+} were found to impinge on the microenvironment (i.e., secondary coordination sphere) of the nickel center. This structural crowding could induce increased reorganization energy penalties or diminish electronic coupling of the redox-active nickel cores with the electrode; in either of these scenarios, k^0 would be diminished as measured. The noted steric crowding effect was quantified in a topographical buried volume analysis that was completed using the SambVca 2.1 webtool developed by Cavallo and co-workers.^{51,52} In this prior work, the percent free volume about the nickel center (denoted $\% V_f$) was diminished only in the cases in which trivalent cations were bound in the crown-like site, due to both the high intrinsic steric demand of triflate as a counteranion as well as the tendency of the crown-based ligand to drive a lateral movement of the cations and their triflates toward the nickel center in a manner that depends on ionic radius. Considering all this, we anticipated that a topographical analysis of the tiara-based $[\text{Ni},\text{M}]^T$ family of complexes would be instructive, particularly from the perspectives that triflate counteranions were used in the new complexes as well as the similar propensity of the tiara ligand to drive lateral movement of the secondary cations toward the nickel center, as shown in Figure 3.

To begin, we first solely considered the structural properties of the isolated Ni(II) complexes in order to compare the monometallic complexes $[\text{Ni},\text{H}_2\text{O}]^T$ and $[\text{Ni},\text{H}_2\text{O}]^C$, as well as the heterobimetallic complexes of K^+ , Sr^{2+} , and Lu^{3+} for which X-ray structural data are available for both ligand systems. This comparison study revealed that the free volume about the Schiff-base site is influenced, to a small degree,⁵³ by the ligand backbones used in the two families of complexes as shown in Figure 11. In accord with the greater tendency of the tiara ligand to drive lateral movement of the secondary cations (and their bound triflates) toward the Schiff-base site, both $[\text{Ni},\text{Sr}]^T$ and $[\text{Ni},\text{Lu}]^T$ have diminished free volume values compared to their analogues $[\text{Ni},\text{Sr}]^C$ and $[\text{Ni},\text{Lu}]^C$ (33.8 vs 37.4 for Sr^{2+} , and 23.4 vs 24.5 vs Lu^{3+}). The diminished free volume about

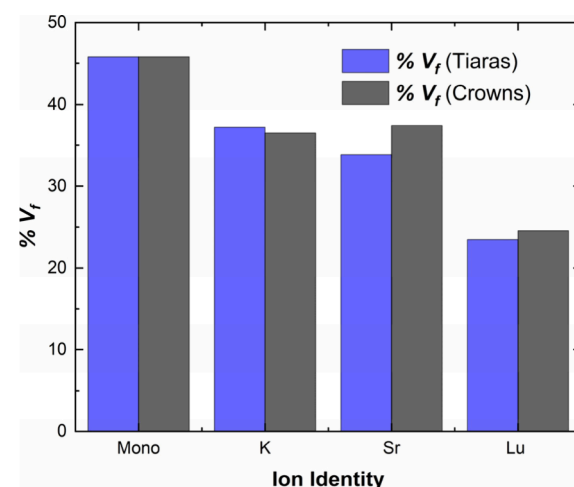


Figure 11. Figure showing a comparison of the $\% V_f$ values for the bitmetallic analogues from both the crown and tiara series. Average values are given for $[\text{Ni},\text{H}_2\text{O}]^T$, $[\text{Ni},\text{Sr}]^T$, and $[\text{Ni},\text{Lu}]^T$, corresponding to the arithmetic mean of the values of $\% V_f$ values calculated from the structural data from XRD analysis.

nickel in the tiara case is sensible given the finding that the triflate counteranions are bound to the secondary cations in all these structures. The free volume values about the nickel centers in the monometallic complexes are also identical in both $[\text{Ni},\text{H}_2\text{O}]^{\text{T}}$ and $[\text{Ni},\text{H}_2\text{O}]^{\text{C}}$, underscoring the structural similarity of the Schiff-base sites in the two ligand systems. $[\text{Ni},\text{K}]^{\text{T}}$ and $[\text{Ni},\text{K}]^{\text{C}}$ display quite similar free volume data (37.2 vs 36.5), featuring only a minor difference that is reflective of the unique structures of the complexes in the solid state; the difference is attributable in part to the preference of K^+ to adopt $\text{CN} = 7$ for $[\text{Ni},\text{K}]^{\text{T}}$ and $\text{CN} = 9$ for $[\text{Ni},\text{K}]^{\text{C}}$. The diminished structural freedom of the crown system appears to drive the lower free volume about nickel in the crown case; the structure of $[\text{Ni},\text{K}]^{\text{C}}$ features a bound triflate that interacts with the K^+ in the uncommon $\kappa^3\text{-[O,O,F]}$ -mode, drawing the triflate closer to the nickel center to satisfy the coordination needs of K^+ in the crown site. By contrast, in the tiara system, triflate binding to K^+ is not preferred, as the polyether site is more flexible and appears to contribute more significantly to filling the coordination sphere of this cation by out-of-plane distortion, as quantified in the ω_{06} parameters for the complexes (Table S6). The K^+ ions in both $[\text{Ni},\text{K}]^{\text{T}}$ and $[\text{Ni},\text{K}]^{\text{C}}$ engage in weak intermolecular interactions that stabilize dimeric structures in the solid state in both cases, but $[\text{Ni},\text{K}]^{\text{T}}$ features an outer-sphere triflate and a marginally greater free volume about nickel as a result.

With this analysis in hand, we then set about estimating the rate of heterogeneous ET to the $[\text{Ni},\text{M}]^{\text{T}}$ complexes with two methods in order to facilitate comparisons to the available structural data. In the first method, the peak-to-peak separation (denoted ΔE_p) was tabulated from the electrochemical data for each heterobimetallic complex in the present study at 100 mV/s. In this approach, faster ET kinetics would be associated with smaller ΔE_p values, as demonstrated in the foundational work from Nicholson.⁵⁴ In the second method, the heterogeneous ET rates (k^0 values) were determined using the traditional, full method from Nicholson that employs a standard working curve to relate measured ΔE_p values quantitatively to k^0 . As in our prior report, values of k^0 were measured at multiple scan rates and tabulated as an average value (Table 2); the average values of k^0 show only minor variation across scan rates, as shown by the modest uncertainties on the values of k^0 shown in Table 2 that were derived from the replicate measurements. As the method of Nicholson was used for determination of k^0 for both the tiara $[\text{Ni},\text{M}]^{\text{T}}$ and crown $[\text{Ni},\text{M}]^{\text{C}}$ complexes, the relationship between k^0 (averaged across multiple scan rates) and ΔE_p (measured at 100 mV/s) was similar in the two cases (Figure S178). This is consistent with both families of complexes having similar diffusion coefficients for their oxidized and reduced forms, and with the suitability of using either the ΔE_p value measured at 100 mV/s or the averaged k^0 value for examining the heterogeneous ET rates. We used both strategies in light of the aforementioned reduction-induced chemical reactivity of the $[\text{Ni},\text{Zn}]^{\text{T}}$ complex, which we anticipated could impact the reliability of k^0 measured across multiple scan rates.

Plotting the k^0 values for the relevant complexes in the $[\text{Ni},\text{M}]^{\text{T}}$ series as a function of the $\text{p}K_a$ value of the incorporated secondary metal cation reveals a nonmonotonic relationship (Figure S179). This nonmonotonic behavior contrasts with what we previously found for the $[\text{Ni},\text{M}]^{\text{C}}$ series, in which structural crowding about the nickel micro-

environment was correlated with diminished ET rates. In the prior work on the crown system, however, we note that the ligand was found to drive a lateral movement of the cations and their associated triflate counteranions; the crown ligand enforces a vectorization of what would normally be a three-dimensional electrostatic effect into the approximately two-dimensional plane of the macrocyclic ligand system. In the $[\text{Ni},\text{M}]^{\text{T}}$ series, the ligand is not macrocyclic and displays more structural freedom than the analogous crown ligand. In both systems, the $[\text{O}_{\text{phen}}\text{--Ni--O}_{\text{phen}}]$ group acts effectively like a large, rigid, and redox-active carboxyl group, and in both systems, the cationic M species, along with their triflate counteranions to some extent, can move in and out along the $\text{Ni}\cdots\text{M}$ vector depending on their ionic radius values (Figure 3). However, in the tiara system of interest here, greater structural degrees of freedom within the ligand system appears to result in a different dependence of the heterogeneous ET rate on the structural properties of the complexes. This is apparent in the plot of the $\%V_f$ values for the tiara systems vs k^0 , which shows a nonmonotonic relationship and shows that $[\text{Ni},\text{Sr}]^{\text{T}}$ has the largest value of k^0 among the tiara-based heterobimetallic complexes (Figure S180). The lack of a monotonic relationship suggests that one or more additional structural factors govern the heterogeneous ET rates displayed by the complexes in the $[\text{Ni},\text{M}]^{\text{T}}$ family.

Inspection of further structural data, however, reveals that there is a reasonable linear correlation between the ΔE_p values (measured at 100 mV/s) for all the heterobimetallic complexes and the $\text{O}1\cdots\text{O}2$ separation measured in the solid-state structures (Figure S185). This indicates that the complexes in which there is the most significant disruption of the structure of the nickel-containing core structure (as quantified by the cation-induced diminishment of $\text{O}1\cdots\text{O}2$ separation, see Tables 1 and 2) are associated with the slowest ET kinetics. The derivatives incorporating Zn^{2+} and Lu^{3+} , which display rather high ΔE_p values, also feature $\%V_f$ values that are the smallest in the full set of data. This may be attributable to the quite significant decreases in the $\text{O}1\cdots\text{O}2$ separation that are induced in the cases of $[\text{Ni},\text{Li}]^{\text{T}}$ and $[\text{Ni},\text{Zn}]^{\text{T}}$, in that upon reduction, there could be significant electrostatic repulsion induced between $\text{O}1$ and $\text{O}2$; reducing $\text{Ni}(\text{II})$ to $\text{Ni}(\text{I})$ would almost certainly cause significant movements of atoms on the lithium and zinc coordination spheres by opening up the common phenoxide polyhedral edge and pushing the polyether arms away. This would result in significant structural reorganization upon reduction and thereby contribute to the diminished ET kinetics.

Along this line of thought, we also examined the k^0 values for both the tiara and crown systems as a function of $\text{O}1\cdots\text{O}2$ separation (Figure S182), but these data do not show a monotonic relationship as might be expected. In particular, the data point for $[\text{Ni},\text{K}]^{\text{T}}$ falls off of the expected relationship, giving an estimated ET rate that is lower than expected given the established relationship between the ΔE_p values (measured at 100 mV/s) and $\text{O}1\cdots\text{O}2$ separation. At this stage, we anticipate that this could be attributable to structural reorganization of the K^+ adduct of the tiara system that would occur upon dissolution of the complex in solvent/electrolyte; such reorganization seems likely given the significant open space in the K^+ coordination sphere that would be opened up by breaking apart the weakly interacting dimeric species that was found in the solid-state data from XRD (see the SI, discussion on p S88, and Figures S140 and

S141). Consequently, we anticipate that in the case of the $[\text{Ni},\text{M}]^{\text{T}}$ complexes, a combination of three factors conspire to result in the unique behavior with respect to heterogeneous ET kinetics in comparison to that found for the $[\text{Ni},\text{M}]^{\text{C}}$ complexes: (1) the $[\text{Ni},\text{M}]^{\text{T}}$ complexes are built upon a ligand with greater structural degrees of freedom; (2) the tiara ligand supports closer approach of incorporated secondary cations to the nickel center than the crown ligand (Figure 3); (3) the tiara ligand enables stable encapsulation and structural characterization of adducts of the small, highly Lewis acidic cations Li^+ and Zn^{2+} . In any case, though, as we have not pursued isolation of the reduced forms of the $[\text{Ni},\text{M}]^{\text{T}}$ complexes, we will not speculate further here regarding the origins of the modulated ET kinetics apart from noting the observed trend between the ΔE_p values and $\text{O}1\cdots\text{O}2$ separation.

DISCUSSION

The nonmacrocyclic tiara ligand system explored in the work described here shows all indications of being a satisfactory replacement for analogous macrocyclic ligands containing crown-ether-like motifs. First, the tiara system reported here can be prepared by a significantly more straightforward synthetic route that is both operationally simpler and requires a shorter time than that required for the analogous crown system. Second, the tiara system reported here appears well suited to generation of diverse heterobimetallic complexes that incorporate a wide range of secondary metal cations. Here, the stable binding of monovalent (K^+ , Na^+ , and Li^+), divalent (Sr^{2+} , Ca^{2+} , and Zn^{2+}), and trivalent cations (La^{3+} and Lu^{3+}) was demonstrated, meaning that a wide range of Lewis acidities (spanning $\text{p}K_a$ values of the corresponding aqua complexes from 7.9 to 16.0), cation sizes (Shannon ionic radii from 0.59 to 1.51 Å), and cation coordination numbers from 5 to 9. This demonstrated ability to form stable heterobimetallics suggests that tiara-type ligand systems could find applications in chemistries in which secondary cations afford tunability to core metal complex structures. Third and finally, the heterobimetallic complexes reported here displayed tunable electronic and electrochemical properties, as quantified through UV-visible absorption spectroscopy and electrochemical measurements. In particular, we highlight that in the findings obtained from both these techniques, satisfactory linear correlations between observed properties (CT transition energy and reduction potential, respectively) and the effective Lewis acidity of the incorporated cation. Thus, the tiara ligand system appears to engender usefully predictable tuning that could be expanded to other cations and/or redox-active metals in future work. All these benefits represent new opportunities to advance the rich area of heterobimetallic chemistry.

In order to facilitate structural, spectroscopic, and electrochemical comparisons between the tiara and crown complexes in the $[\text{Ni},\text{M}]^{\text{T}}$ and $[\text{Ni},\text{M}]^{\text{C}}$ families, 1,1-dimethyl-1,2-ethylenediamine was used to install the diimine bridge at the Schiff-base site in both sets of complexes. Additionally, to facilitate comparison of heterobimetallic species that differ only by the composition of the polyether site, we prepared complexes incorporating K^+ , Sr^{2+} , and Lu^{3+} to compare across the two ligand systems; we could also compare the structures of the corresponding monometallic complexes $[\text{Ni},\text{H}_2\text{O}]^{\text{T}}$ and $[\text{Ni},\text{H}_2\text{O}]^{\text{C}}$. When the structures of the monometallic complexes are superimposed, the closed related nature of the two complexes becomes readily apparent (Figure 12a). Both

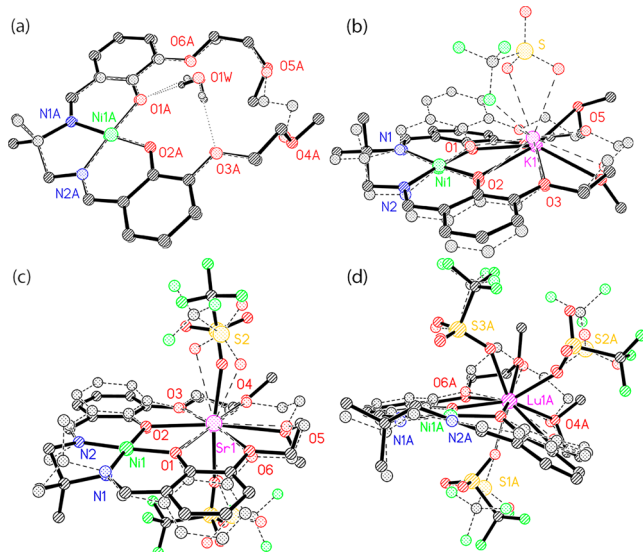


Figure 12. Superimposed solid-state structures of the $[\text{Ni},\text{M}]^{\text{T}}$ and $[\text{Ni},\text{M}]^{\text{C}}$ species for which analogous derivatives are available. For each pair of structures, the weighted RMSD of the positions of atoms Ni, N1, N2, O1, O2, O3, O4, O5, and O6 were calculated; the secondary cation M was also included in the RMSD calculation for the heterobimetallic complexes. Structures: (a) $[\text{Ni},\text{H}_2\text{O}]^{\text{T}}$ and $[\text{Ni},\text{H}_2\text{O}]^{\text{C}}$, RMSD = 0.159 Å; (b) $[\text{Ni},\text{K}]^{\text{T}}$ and $[\text{Ni},\text{K}]^{\text{C}}$, RMSD = 0.440 Å; (c) $[\text{Ni},\text{Sr}]^{\text{T}}$ and $[\text{Ni},\text{Sr}]^{\text{C}}$, RMSD = 0.128 Å; (d) $[\text{Ni},\text{Lu}]^{\text{T}}$ and $[\text{Ni},\text{Lu}]^{\text{C}}$, RMSD = 0.158 Å. Solid bonds to atoms shaded bottom left to top right are shown for the tiara structures, while dashed bonds to atoms with a regular dot pattern are shown for the crown structures.

complexes feature rigorously square planar Schiff-base sites, and also feature water molecules engaged in H-bonding interactions with one phenoxide oxygen atom and one ethereal oxygen atom in the polyether site. The weighted RMSD of the atoms Ni, N1, N2, O1, O2, O3, O4, O5, and O6 between the two structures is only 0.159 Å, in accord with the recognized influence of the Schiff-base site in both complexes to promote coplanarity among the oxygen atoms of the polyether sites in both cases ($\omega_{\text{O}6} = 0.255$ and 0.245 for the $[\text{Ni},\text{H}_2\text{O}]^{\text{T}}$ and $[\text{Ni},\text{H}_2\text{O}]^{\text{C}}$, respectively). The bound water molecules could also assist in enforcing the similar conformations of these complexes in the solid state. The heterobimetallic complexes based on Sr^{2+} and Lu^{3+} are similar in the tiara and crown systems in both cases, with RMSD values comparing the positions of atoms Ni, M, N1, N2, O1, O2, O3, O4, O5, and O6 being only 0.128 and 0.159 Å in the two cases. $[\text{Ni},\text{Sr}]^{\text{T}}$ and $[\text{Ni},\text{Sr}]^{\text{C}}$ are the most similar across the series of comparable complexes, a feature attributable to the placement of one triflate on each hemisphere of the strontium cation in each case. This motif appears to enforce coplanarity of the oxygen atoms in the polyether site, a tendency that should contribute to the modest RMSD for the structures compared here. $[\text{Ni},\text{Lu}]^{\text{T}}$ and $[\text{Ni},\text{Lu}]^{\text{C}}$ appear quite similar to each other as well; two triflates are bound in the κ^1 mode to Lu^{3+} on one hemisphere while the third triflate is bound on the opposite hemisphere in the κ^1 mode. In both cases, the greater steric bulk on the first hemisphere that is driven by the binding of two triflates appears to engender a preference for the conformations of the diimine bridge of the Schiff-base site (Figures S158 and S161) to feature one pseudoaxial methyl group that faces toward the hemisphere of the lutetium center

that contains only one bound triflate. On steric grounds, this structural feature found for $[\text{Ni},\text{Lu}]^T$ and $[\text{Ni},\text{Lu}]^C$ can be concluded to promote satisfactory solid-state packing.

We note that the symmetric bihemispheric triflate binding motif has been observed previously in derivatives $[\text{Ni},\text{Ca}]^C$,²² $[\text{Pd},\text{Ca}]^C$,²² and $[\text{Pd},\text{Sr}]^C$ as well,²² but in the calcium cases, the formation of this motif resulted in significant crystallographic disorder. In the case of $[\text{Ni},\text{Sr}]^T$, we also note that a disorder pattern was encountered in which the triflate (associated with S2) of the major cocrystallized isomer of the complex was found to be bound to Sr^{2+} in the κ^1 mode (shown in Figure 12, structure c), while the minor cocrystallized isomer features the same triflate bound to Sr^{2+} in the κ^2 mode. We were initially surprised to note that the related triflate in $[\text{Ni},\text{Sr}]^C$ did not display disorder and was found to be bound to Sr^{2+} only in the κ^2 mode; thus, we sought to identify another interaction with the triflate that might prompt the preference for the κ^1 binding mode in the major isomer of $[\text{Ni},\text{Sr}]^T$. On close inspection of the structural data, the triflate associated with S2 in the major isomer of $[\text{Ni},\text{Sr}]^T$ was found to be engaged in an intrinsically weak C–H···O hydrogen bond with the terminal methyl group (associated with C11) of the nearby polyether arm (Figure S153). This interaction appears to be inaccessible in the analogous complex $[\text{Ni},\text{Sr}]^C$ based on the crown platform, owing to both the more tightly enforced coplanarity of the atoms in the macrocyclic crown-like site and also the replacement of the terminal methyl groups with a bridging ethylene moiety that appears unable to reach upward sufficiently far to directly interact with the corresponding triflate oxygen atoms. It appears that a subtle conformational shift occurs when the triflate interacts directly with the polyether site via this intrinsically weak C–H···O hydrogen bond, because the atomic displacement ellipsoid for O5 is distorted in the final model for $[\text{Ni},\text{Sr}]^T$, suggestive of corresponding conformations of the tiara ligand being present in the solid state but not sufficiently resolved in the data to be modeled appropriately for full correlation with the unique triflate positions of the major and minor cocrystallized isomers that were found in the same volume of the asymmetric unit. The observation of this subtle conformational flexibility of the polyether site in the tiara ligand further supports the conclusion that this ligand features greater degrees of freedom than the crown analogue.

The work described here was inspired in large measure by the work of Soo and co-workers.^{33–35} In this work, the structures of several complexes were reported that are based upon heteroditopic tiara-type ligands. Like those reported here, the complexes from Soo and co-workers feature nickel(II) centers in Schiff-base sites and polyether sites based upon six oxygen donors. However, the complexes from Soo and co-workers feature fully conjugated salophen-type Schiff-base sites bridged by phenylenediamine moieties rather than unconjugated, aliphatic diamine bridges as employed in the complexes reported here. This change in diimine bridge does not appear to affect the validity of the general conclusions that we have established using the new family of tiara structures reported here. For example, in the two structures of monometallic nickel complexes reported by Soo and co-workers, the ω_{O6} values corresponding to the polyether sites are 0.249 in a structure from 2016 and 0.63(9) for a disordered structure from 2019 (Figure S183). The observation that the coplanarity of the oxygen atoms in the polyether site can vary so greatly underscores the conformational flexibility of the

polyether site within the tiara framework. Soo and co-workers have also reported structures of heterobimetallic complexes incorporating K^+ (Figure S184). In one of these, K^+ features $\text{CN} = 8$, a $\text{Ni}\cdots\text{M}$ distance of 3.730 Å, and an ω_{tiara} value of 0.284. In $[\text{Ni},\text{K}]^T$, the ω_{tiara} value is greater at 0.534, but the structure features K^+ with $\text{CN} = 7$ and a $\text{Ni}\cdots\text{M}$ distance of 3.704 Å. The greater ω_{O6} value in our structure is attributable to the triflate counteranion being located in the outer coordination sphere. As with the structure from Soo and co-workers, the corresponding PF_6^- is located in the inner coordination sphere and interacts with K^+ in the κ^2 mode via bridging fluorine atoms; binding of the PF_6^- in an inner-sphere fashion likely contributes to pushing the oxygen atoms of the polyether site into the ligand plane. Supporting this conclusion, we also examined the other heterobimetallic structure from Soo and co-workers that features a bound K^+ cation in a tiara-type ligand; in this other case, K^+ features $\text{CN} = 9$, a $\text{Ni}\cdots\text{M}$ distance of 3.746 Å, and an ω_{O6} value of 0.289. In this structure, the PF_6^- counteranion is bound in the inner coordination sphere to K^+ via three bridging fluorine atoms, increasing the formal CN of K^+ to 9. Nonetheless, the $\text{Ni}\cdots\text{M}$ distance and ω_{O6} values are similar to those found in the other structures. Specifically, we note that the observation of $\text{Ni}\cdots\text{M}$ distances that span a narrow range of less than 0.05 Å supports our general conclusion that secondary cations prefer to nestle into the nascent diamond core motif defined by the two phenoxide oxygen atoms in both the tiara and crown ligand systems. This preference likely strongly influences the cation-driven tuning properties of complexes based on these ligand systems, and the ability of these ligands to successfully bind a variety of secondary cations. Along this line, we have recently reported stable binding of the uranyl dication in the polyether site of $[\text{Pt}]^C$, a phenomenon that appears to be promoted by both the partial anionic character of the phenoxide oxygen atoms in the monometallic precursor and the coplanarity of the oxygen atoms in the crown-like-site that is enforced by the metal-containing accessory Schiff-base site.²²

Most recently, Williams and co-workers reported the solid-state structures of three heterobimetallic cobalt(III) complexes based on a tiara-type ligand.³⁶ The derivatives from Williams and co-workers feature an aliphatic diimine bridge in the Schiff-base site of the tiara ligand, but much like in the structures from Soo and co-workers, two polyether arms that define a site with a total of six oxygen donors. The structures from Williams and co-workers are intriguing for comparison to those reported here, because they feature acetate counteranions in all cases that balance both the positive charges associated with the cobalt(III) center and the incorporated secondary metal cations. These derivatives were prepared only with monovalent cations, namely Na^+ , K^+ , and Rb^+ ; Williams and co-workers found that these species displayed attractive properties for studies of low-pressure propylene oxide and carbon dioxide ring opening polymerization catalysis. However, despite the disparate features of their acetate counteranions and our triflate counteranions, comparison of the available structures to our own confirms similar structural trends in each case. Comparing the adducts of Na^+ , K^+ , and Rb^+ in the Williams tiara ligand, the ω_{tiara} values are 1.038, 0.271, and 0.269; this trend of greater out-of-plane deviation for the oxygen atoms in the polyether site is in accord with our findings here, confirming that even in the presence of strongly coordinating acetate, the tiara ligand motif displays substantial ability for encapsulation of small cations like Na^+ (Figure

S115). The Co···M distances of 3.282, 3.750, and 3.875 Å in the Williams tiaras with bound Na⁺, K⁺, and Rb⁺, respectively are also in accord with our finding of ionic-radius dependent intermetallic separation in the [Ni,M]^T complexes; for the Williams complexes, a linear relationship between ionic radius and Co···M separation was measured, with a unitless slope of 1.207 ± 0.008 (Figure S186). This value is significantly higher than that found for the [Ni,M]^T series of 0.95 ± 0.01 , likely due to the presence of one bridging acetate counteranion in each of the Williams complexes. The bridging counteranion could effectively pull the cobalt center and the associated secondary metal cation closer together in each case. The observation of this linear relationship, in any case, underscores that the behaviors measured in our [Ni,M]^T and [Ni,M]^C systems are not artifacts of any of the specific features of our complexes (selection of Ni(II) for placement in the Schiff-base site; utilization of triflate salts of the secondary cations; inclusion of the two methyl groups on the diimine backbone to facilitate synthesis of the monometallic precursors [Ni]^T and [Ni]^C). Taking all these structural results together, we conclude that our findings discussed here are general in nature, and could be used to understand behaviors in structurally analogous tiara-type heteroditopic ligands as well as in heterobimetallic derivatives based upon different cations with triflates or different salts entirely that feature anions that might be substantially different from triflate.

The results in this work are potentially impactful because of the recognized usefulness of heteroditopic ligands for the binding of two or more metal cations to study of heterobimetallic chemistry. Some ligands used for this purpose have tended until the present to be based on macrocyclic systems that are less flexible and impose possibly significant restrictions on metal coordination numbers and geometries. In the work presented here, the relaxation of one of these restrictions, namely the macrocyclic nature of the ligand and the crown-ether-like nature of the polyether site, was found to result in only minor perturbations of the structures of the heterobimetallic complexes. Likely as a consequence of these similar structural properties, similar spectroscopic and electrochemical findings for both the new nonmacrocyclic complexes based on the tiara motif and the prior macrocyclic complexes based on the crown motif were obtained across the full series. Generally, the coordination number of M was found to be decreased in the case of the tiara complexes, likely a consequence of the more flexible tiara polyether environment. However, the reduction in coordination number in the tiara family is probably more directly a consequence of eliminating one ethylene linker from the prototypical crown motif. Removal of this linker removes the macrocyclic effect that constrains the O4···O5 separation in the crown system to be a 4-atom “bite”. One could promote higher coordination numbers for cations by using compact bidentate (or higher denticity) anionic ligands; space on the metal coordination sphere is almost certainly the critical factor in determining whether monodentate or bidentate triflates occur in these structures. Triflate presents a small three-atom bite (in principle, at least) but it is not as ideally shaped or as compact as other candidate ligands (e.g., acetate, nitrate) to promote high coordination numbers.

In both the tiara and crown complexes, the ligands promote lateral movement of the cations with respect to the Schiff-base site containing nickel that is dependent on their ionic radii. [Ni]^T and [Ni]^C take what would conventionally be three-

dimensional electrostatic effects between cations interacting through two or more bridging ligands and constrain them by vectorization into approximately two-dimensional planes defined by the structures of [Ni]^T and [Ni]^C. This work thus highlights that macrocyclic ligands may not be required for all applications in heterobimetallic chemistry; desirable results are clearly obtainable with more flexible systems, particularly in cases where bridging ligands with partial anionic character may be present to guide the formation of heterometallic cores. We anticipate that an appealing direction for future research could include examination of ligand variations that modulate the anionic character of such bridging groups, an approach that could directly examine the role of bridging ligands in mediating the conceptual metal-to-metal communication in heterobimetallic species. Examination of such influences on the vectorization of cation-induced effects is currently underway in our laboratory.

CONCLUSION

In this work, a series of nickel-based heterobimetallic complexes were prepared with a nonmacrocyclic ligand that presents a polyether site that has been found suitable for the binding of mono-, di-, and trivalent metal cations (M). The solid-state structures of the complexes reveal that the Ni···M distance is driven by the ionic radius of the secondary metal cations, mirroring results obtained previously in macrocyclic ligands in which the polyether site is defined with a crown-ether-like cyclic structure. The acyclic polyether moiety in the ligand reported here, dubbed a tiara motif in recognition of its structural similarity to the more commonly studied crown motif, performed quite similarly when comparing spectroscopic and electrochemical results to prior studies with crown ethers. This similar level of performance can be attributed to the similar structures of the heterobimetallic species based upon the tiara and crown complexes surveyed here, highlighting a role for anionic character on bridging phenoxide ligands in driving the properties of the heterobimetallic cores assembled with both ligands. As substantial “tuning power” can be obtained from incorporated secondary metal cations when using the nonmacrocyclic ligand reported here, such ligands can be concluded to represent an attractive general class that is worthy of further development for applications in the field of tunable heterobimetallic chemistry.

EXPERIMENTAL SECTION

General Considerations. All manipulations were carried out in dry N₂-filled gloveboxes (Vacuum Atmospheres Co., Hawthorne, CA) or under a N₂ atmosphere using standard Schlenk techniques unless otherwise noted. All solvents were of commercial grade, and those used in air-free conditions were dried over activated alumina using a PPT Glass Contour (Nashua, NH) solvent purification system prior to use and stored over molecular sieves. All chemicals were purchased from major commercial suppliers and used as received or after extensive drying. 2,3-Dihydroxybenzaldehyde was sublimed in *vacuo* before use. CD₃CN was purchased from Cambridge Isotope Laboratories and dried over 3 Å molecular sieves. ¹H, ¹³C, and ¹⁹F NMR spectra were collected on a 500 MHz Bruker spectrometer and referenced to the residual protio-solvent signal in the case of ¹H and ¹³C. ¹⁹F NMR spectra were referenced and reported relative to CCl₃F as an external standard following the recommended scale based on ratios of absolute frequencies (Ξ). Chemical shifts (δ) are reported in units of ppm and coupling constants (J) are reported in Hz. NMR spectra are given in Figures S1–S26. Electronic absorption spectra were collected with an Ocean Optics Flame spectrometer, in a 1 cm

path length quartz cuvette. Elemental analysis results for $[\text{Ni}]^T$ and the series of complexes $[\text{Ni},\text{M}]^T$ (where $\text{M} = \text{K}^+, \text{Na}^+, \text{Li}^+, \text{Sr}^{2+}, \text{Ca}^{2+}, \text{Zn}^{2+}, \text{La}^{3+}$, and Lu^{3+}) were provided by Midwest Microlab, Inc. (Indianapolis, IN), the samples for which were dried in vacuo at 60 °C overnight. Details on the use of the SambVca 2.1 webtool can be found in a prior report²² and are discussed in the SI, p S136.

Electrochemistry. Electrochemical experiments were carried out in a N_2 -filled glovebox in dry, degassed CH_3CN . 0.10 M tetra(*n*-butylammonium) hexafluorophosphate ($[\text{nBu}_4\text{N}]^+[\text{PF}_6]^-$; Sigma-Aldrich, electrochemical grade) served as the supporting electrolyte. Measurements were made with a Gamry Reference 600+ potentiostat/galvanostat using a standard three-electrode configuration. The working electrode was the basal plane of highly oriented pyrolytic graphite (HOPG; GraphiteStore.com, Buffalo Grove, IL; surface area = 0.09 cm^2), the counter electrode was a platinum wire (Kurt J. Lesker, Jefferson Hills, PA; 99.99%, 0.5 mm diameter), and a silver wire immersed in an electrolyte served as a pseudoreference electrode (CH Instruments). The reference was separated from the working solution by a Vycor frit (Bioanalytical Systems, Inc.). Ferrocene (Sigma-Aldrich; twice-sublimed) was added to an electrolyte solution not containing the compounds tested prior to the beginning of each experiment; the midpoint potential of the ferrocenium/ferrocene couple (denoted as $\text{Fc}^{+/0}$) served as an external standard for comparison of the recorded potentials. The concentrations of the analyte for cyclic voltammetry was ca. 2 mM unless otherwise noted. Compensation for solution resistance (measured by impedance spectroscopy to be small, ca. 110–150 Ω) was not carried out for any of the data presented here; based on preliminary comparisons, the data quality was higher without applying compensation.

Synthesis and Characterization. Caution! Sodium hydride (NaH) and hydrochloric acid (HCl) are used to prepare 3-(2-methoxyethoxy)-2-hydroxybenzaldehyde. NaH is a flammable solid. Hydrogen gas is released upon contact of NaH with water, and the gas may ignite spontaneously. NaH causes severe skin burns and eye damage. Store in a dry place and in a closed container with a corrosion-resistant liner. Hydrochloric acid (HCl) is a corrosive and strong acid. Metal instruments may be damaged upon contact with HCl . HCl causes severe skin burns and eye damage. Store and use HCl in appropriate containers that are corrosion-resistant. Wear protective gloves, a suitable laboratory coat, and eye protection when using NaH and/or HCl .

Synthesis of 3-(2-Methoxyethoxy)-2-hydroxybenzaldehyde. This compound has been previously reported, and the currently reported synthesis is adapted from a source in the literature.³³ Under an inert nitrogen atmosphere, a dried Schlenk flask was loaded with 0.58 g (24 mmol) of NaH . To this mass was added 5 mL of dry THF to form a suspension. Under a light flow of nitrogen and with an ice bath was added dropwise a solution consisting of 1.5 g (11 mmol) of 2,3-dihydroxybenzaldehyde and 20 mL of THF over the course of 1 h. After this addition, the solution was left to stir without the ice bath for an additional 1.5 h. A solution of 2.58 g (0.11 mmol) of 2-methoxyethyl-*p*-toluenesulfonate diluted to 20 mL with THF was then added slowly to the Schlenk flask. After an additional 30 min of nitrogen flow, the flask was sealed and allowed to stir react for 96 h under heating to 40 °C, eventually forming a deep-yellow, opaque solution. After stirring, any extra NaH was quenched with the addition of 110 mL of water causing a color change to dark brown. This solution was extracted twice with chloroform to remove any unreacted organic material. The aqueous layer was then acidified to a pH of 2 using 6 M HCl. After acidification, another extraction was done with chloroform. The organic layer was then washed with 1 M HCl and dried with MgSO_4 . The chloroform was removed in vacuo until an orange oil remained, which solidified on standing at room temperature and was used without further purification. Yield: 82%. Spectroscopic characterization via ^1H NMR are in agreement with similar complexes from the literature.³³

Synthesis of $[\text{Ni}]^T$. To a round-bottom flask were added 1 g (5 mmol) of 3-(2-methoxyethoxy)-2-hydroxybenzaldehyde, 0.225 g (2.6 mmol) of 1,2-diamino-2-methylpropane, and 0.634 g (2.6 mmol) of $\text{Ni}(\text{OAc})_2 \cdot 4\text{H}_2\text{O}$ all dissolved in 100 mL of ethanol. This reaction was allowed to stir and reflux for 20 h, after which the ethanol was

removed in vacuo. The material was then dissolved in a minimal amount of CHCl_3 and triturated with cold ether to precipitate the product, which was then obtained via vacuum filtration over a frit. Crystals suitable for XRD were obtained under an ambient atmosphere via diffusion of pentane into chloroform at –20 °C.

$[\text{Ni}]^T$. Yield: 75.2%. ^1H NMR (500 MHz, CD_3CN): δ 7.61 (s, 1H, H3), 7.59 (s, 1H, H3), 6.92 (d, $^3J_{\text{H},\text{H}} = 7.45$ Hz, 1H, H4), 6.85 (d, $^3J_{\text{H},\text{H}} = 7.93$ Hz, 1H, H4), 6.79 (d, $^3J_{\text{H},\text{H}} = 7.58$ Hz, 2H, H6), 6.45 (t, $^3J_{\text{H},\text{H}} = 7.48$ Hz, 1H, HS), 6.43 (t, $^3J_{\text{H},\text{H}} = 7.45$ Hz, 1H, HS), 4.08 (m, 4H, H7), 3.65 (m, 4H, H8), 3.35 (s, 6H, H9), 3.25 (s, 2H, H2), 1.45 (s, 6H, H1). $^{13}\text{C}\{^1\text{H}\}$ NMR (126 MHz, CD_3CN): δ 136.28, 160.23, 157.48, 156.87, 150.88, 150.75, 126.54, 125.91, 122.05, 121.85, 117.82, 117.66, 114.67, 71.99, 71.53, 68.93, 68.87, 66.76, 58.99, 25.86. Anal. Calcd for $\text{C}_{24}\text{H}_{30}\text{N}_2\text{O}_6\text{Ni}$ ($[\text{Ni}]^T$): C, 57.51; H, 6.03; N, 5.59. Found: C, 55.60; H, 5.86; N, 5.64. Calcd for $\text{C}_{24}\text{H}_{30}\text{N}_2\text{O}_6\text{Ni} \cdot 0.75\text{H}_2\text{O}$: C, 56.00; H, 6.17; N, 5.64. Water inclusion in the sample likely resulted from shipping, as this complex can bind water as seen in the crystal structure. Cyclic voltammetry (0.1 M $[\text{nBu}_4\text{N}]^+[\text{PF}_6]^-$ in CH_3CN): $E_{1/2} = -2.10$ V vs $\text{Fc}^{+/0}$. Electronic absorption spectrum in CH_3CN ($\text{M}^{-1} \text{cm}^{-1}$): 418 (5853) nm.

Synthesis of $[\text{Ni},\text{M}]^T$ Heterobimetallic Complexes. Under an inert atmosphere of nitrogen to a solution of 100 mg of $[\text{Ni}]^T$ in ~5 mL of MeCN, a solution of $\text{M}(\text{OTf})_n$ in ~5 mL of MeCN was added and stirred for at least 30 min. The solvent was removed in vacuo and the product was milled. Yields were virtually quantitative in all cases. Crystals suitable for XRD for compounds $[\text{Ni},\text{K}]^T$, $[\text{Ni},\text{Li}]^T$, $[\text{Ni},\text{Sr}]^T$, and $[\text{Ni},\text{Zn}]^T$ were obtained via a vapor diffusion of Et_2O into MeCN. Suitable crystals for compound $[\text{Ni},\text{Lu}]^T$ were obtained via diffusion of CH_2Cl_2 into CH_3CN at –30 °C for several months.

$[\text{Ni},\text{K}]^T$. Yield: 96%. ^1H NMR (500 MHz, CD_3CN): δ 7.65 (s, 1H, H3), 7.64 (s, 1H, H3), 6.99 (d, $^3J_{\text{H},\text{H}} = 8.00$ Hz, 1H, H4), 6.92 (d, $^3J_{\text{H},\text{H}} = 8.00$ Hz, 1H, H4), 6.89 (d, $^3J_{\text{H},\text{H}} = 7.80$ Hz, 2H, H6), 6.59 (t, $^3J_{\text{H},\text{H}} = 7.90$ Hz, 1H, HS), 6.58 (t, $^3J_{\text{H},\text{H}} = 7.85$ Hz, 1H, HS), 4.10 (m, 4H, H7), 3.73 (m, 4H, H8), 3.38 (s, 6H, H9), 3.28 (s, 2H, H2), 1.48 (s, 6H, H1). $^{13}\text{C}\{^1\text{H}\}$ NMR (126 MHz, CD_3CN): δ 164.16, 161.13, 155.01, 154.35, 149.94, 149.83, 126.54, 125.95, 121.69, 121.50, 115.83, 115.80, 115.56, 71.49, 70.73, 67.37, 67.25, 58.59, 25.76. ^{19}F NMR (470 MHz, CD_3CN): δ –80.18. Anal. Calcd for $\text{C}_{25}\text{H}_{30}\text{N}_2\text{O}_9\text{F}_3\text{SNIK}$ ($[\text{Ni},\text{K}]^T$): C, 43.56; H, 4.39; N, 4.06. Found: C, 43.19; H, 4.44; N, 4.11. Cyclic voltammetry (0.1 M $[\text{nBu}_4\text{N}]^+[\text{PF}_6]^-$ in CH_3CN): $E_{1/2} = -1.94$ V vs $\text{Fc}^{+/0}$. Electronic absorption spectrum in CH_3CN ($\text{M}^{-1} \text{cm}^{-1}$): 409 (6700) nm.

$[\text{Ni},\text{Na}]^T$. Yield: 95%. ^1H NMR (500 MHz, CD_3CN): δ 7.74 (s, 1H, H3), 7.72 (s, 1H, H3), 7.08 (d, $^3J_{\text{H},\text{H}} = 8.05$ Hz, 1H, H4), 7.01 (d, $^3J_{\text{H},\text{H}} = 8.05$ Hz, 3H, H4 H6), 6.62 (t, $^3J_{\text{H},\text{H}} = 7.95$ Hz, 1H, HS), 6.61 (t, $^3J_{\text{H},\text{H}} = 7.80$ Hz, 1H, HS), 4.15 (m, 4H, H7), 3.64 (m, 4H, H8), 3.14 (s, 6H, H9), 3.36 (s, 2H, H2), 1.50 (s, 6H, H1). $^{13}\text{C}\{^1\text{H}\}$ NMR (126 MHz, CD_3CN): δ 164.06, 161.04, 155.25, 154.66, 149.48, 149.36, 127.47, 126.88, 121.94, 121.76, 118.95, 118.88, 116.20, 71.36, 70.90, 69.89, 69.86, 67.80, 59.22, 25.86. ^{19}F NMR (470 MHz, CD_3CN): δ –80.18. Anal. Calcd for $\text{C}_{25}\text{H}_{30}\text{N}_2\text{O}_9\text{F}_3\text{SNIa}$ ($[\text{Ni},\text{Na}]^T$): C, 44.60; H, 4.49; N, 4.16. Found: C, 44.20; H, 4.71; N, 4.16. Cyclic voltammetry (0.1 M $[\text{nBu}_4\text{N}]^+[\text{PF}_6]^-$ in CH_3CN): $E_{1/2} = -1.91$ V vs $\text{Fc}^{+/0}$. Electronic absorption spectrum in CH_3CN ($\text{M}^{-1} \text{cm}^{-1}$): 406 (6466) nm.

$[\text{Ni},\text{Li}]^T$. Yield: 98%. ^1H NMR (500 MHz, CD_3CN): δ 7.78 (s, 1H, H3), 7.77 (s, 1H, H3), 7.19 (d, $^3J_{\text{H},\text{H}} = 7.85$ Hz, 1H, H4), 7.17 (d, $^3J_{\text{H},\text{H}} = 7.60$ Hz, 2H, H6), 7.12 (d, $^3J_{\text{H},\text{H}} = 8.05$ Hz, 1H, H4), 6.70 (t, $^3J_{\text{H},\text{H}} = 7.80$ Hz, 1H, HS), 6.69 (t, $^3J_{\text{H},\text{H}} = 7.85$ Hz, 1H, HS), 4.17 (m, 4H, H7), 3.59 (m, 4H, H8), 3.43 (s, 6H, H9), 3.39 (s, 2H, H2), 1.52 (s, 6H, H1). $^{13}\text{C}\{^1\text{H}\}$ NMR (126 MHz, CD_3CN): δ 164.45, 161.43, 154.88, 149.41, 149.27, 129.35, 128.75, 124.36, 122.44, 122.27, 117.44, 73.08, 71.37, 71.22, 68.28, 59.63, 25.78. ^{19}F NMR (470 MHz, CD_3CN): δ –80.16. Anal. Calcd for $\text{C}_{25}\text{H}_{30}\text{N}_2\text{O}_9\text{F}_3\text{SNI Li}$ ($[\text{Ni},\text{Li}]^T$): C, 45.69; H, 4.60; N, 4.26. Found: C, 45.43; H, 4.66; N, 4.57. Cyclic voltammetry (0.1 M $[\text{nBu}_4\text{N}]^+[\text{PF}_6]^-$ in CH_3CN): $E_{1/2} = -1.83$ V vs $\text{Fc}^{+/0}$. Electronic absorption spectrum in CH_3CN ($\text{M}^{-1} \text{cm}^{-1}$): 395 (5457) nm.

[Ni,Sr]^T. Yield: 98%. ¹H NMR (500 MHz, CD₃CN): δ 7.73 (s, 1H, H3), 7.72 (s, 1H, H3), 7.13 (d, $^3J_{H,H}$ = 7.95 Hz, 1H, H4), 7.05 (d, $^3J_{H,H}$ = 8.00 Hz, 1H, H4), 7.04 (d, $^3J_{H,H}$ = 7.90 Hz, 2H, H6), 6.76 (t, $^3J_{H,H}$ = 7.95 Hz, 1H, H5), 6.74 (t, $^3J_{H,H}$ = 7.90 Hz, 1H, H5), 4.27 (m, 4H, H7), 3.92 (m, 4H, H8), 3.54 (s, 6H, H9), 3.35 (s, 2H, H2), 1.52 (s, 6H, H1). ¹³C{¹H} NMR (126 MHz, CD₃CN): δ 164.96, 161.85, 151.68, 151.00, 148.66, 148.54, 127.43, 126.89, 121.42, 121.24, 117.55, 116.12, 71.25, 70.93, 70.88, 68.06, 67.02, 66.99, 59.83, 59.79. ¹⁹F NMR (470 MHz, CD₃CN): δ -79.98. Anal. Calcd for C₂₆H₃₀N₂O₁₂F₆S₂NiSr ([Ni,Sr]^T): C, 35.21; H, 3.41; N, 3.16. Found: C, 34.81; H, 3.52; N, 3.17. Cyclic voltammetry (0.1 M [nBu₄N]⁺[PF₆]⁻ in CH₃CN): $E_{1/2}$ = -1.70 V vs Fc^{+/-}. Electronic absorption spectrum in CH₃CN (M⁻¹ cm⁻¹): 392 (5978) nm.

[Ni,Ca]^T. Yield: 99%. ¹H NMR (500 MHz, CD₃CN): δ 7.75 (s, 1H, H3), 7.75 (s, 1H, H3), 7.18 (d, $^3J_{H,H}$ = 8.05 Hz, 1H, H4), 7.09 (d, $^3J_{H,H}$ = 7.95 Hz, 3H, H4 and H6), 6.78 (t, $^3J_{H,H}$ = 7.95 Hz, 1H, H5), 6.77 (t, $^3J_{H,H}$ = 7.90 Hz, 1H, H5), 4.35 (m, 4H, H7), 3.88 (m, 4H, H8), 3.56 (s, 3H, H9), 3.55 (s, 3H, H9), 3.37 (s, 2H, H2), 1.52 (s, 6H, H1). ¹³C{¹H} NMR (126 MHz, CD₃CN): δ 164.77, 161.57, 150.61, 148.27, 148.10, 127.75, 127.12, 121.51, 121.29, 117.84, 117.82, 117.09, 116.81, 71.13, 71.04, 70.95, 68.41, 67.95, 67.77, 60.33, 25.53. ¹⁹F NMR (470 MHz, CD₃CN): δ -79.98. Anal. Calcd for C₂₆H₃₀N₂O₁₂F₆S₂NiCa ([Ni,Ca]^T): C, 37.20; H, 3.60; N, 3.34. Found: C, 37.60; H, 3.79; N, 3.53. Cyclic voltammetry (0.1 M [nBu₄N]⁺[PF₆]⁻ in CH₃CN): $E_{1/2}$ = -1.69 V vs Fc^{+/-}. Electronic absorption spectrum in CH₃CN (M⁻¹ cm⁻¹): 389 (5679) nm.

[Ni,Zn]^T. Yield: 99%. ¹H NMR (500 MHz, CD₃CN): δ 7.88 (s, 1H, H3), 7.87 (s, 1H, H3), 7.32 (d, $^3J_{H,H}$ = 8.10 Hz, 1H, H4), 7.27 (d, $^3J_{H,H}$ = 7.55 Hz, 2H, H6), 7.25 (d, $^3J_{H,H}$ = 7.55 Hz, 1H, H4), 6.88 (t, $^3J_{H,H}$ = 8.05 Hz, 1H, H5), 6.88 (t, $^3J_{H,H}$ = 8.00 Hz, 1H, H5), 4.38 (m, 4H, H7), 3.90 (m, 4H, H8), 3.62 (s, 6H, H9), 3.53 (s, 2H, H2), 1.55 (s, 6H, H1). ¹³C{¹H} NMR (126 MHz, CD₃CN): δ 165.07, 162.16, 148.98, 148.49, 146.62, 146.50, 128.99, 128.38, 122.33, 122.18, 119.25, 71.66, 71.46, 70.23, 69.99, 69.67, 61.56, 25.74. ¹⁹F NMR (470 MHz, CD₃CN): δ -80.14. Anal. Calcd for C₂₆H₃₀N₂O₁₂F₆S₂NiZn ([Ni,Zn]^T): C, 36.11; H, 3.50; N, 3.24. Found: C, 36.01; H, 3.99; N, 3.32. Calcd for C₂₆H₃₀N₂O₁₂F₆S₂NiZn-0.65H₂O: C, 35.63; H, 3.60; N, 3.20. Water inclusion in the sample likely resulted from shipping, as the bimetallic complexes in the family reported here are hygroscopic. Cyclic voltammetry (0.1 M [nBu₄N]⁺[PF₆]⁻ in CH₃CN): $E_{1/2}$ = -1.54 V vs Fc^{+/-}. Electronic absorption spectrum in CH₃CN (M⁻¹ cm⁻¹): 376 (5822) nm.

[Ni,La]^T. Yield: 100%. ¹H NMR (500 MHz, CD₃CN): δ 8.09 (s, 1H, H3), 8.05 (s, 1H, H3), 7.27 (d, $^3J_{H,H}$ = 8.00 Hz, 1H, H4), 7.20 (d, $^3J_{H,H}$ = 8.05 Hz, 2H, H6), 7.18 (d, $^3J_{H,H}$ = 7.95 Hz, 1H, H4), 6.94 (t, $^3J_{H,H}$ = 7.95 Hz, 1H, H5), 6.91 (t, $^3J_{H,H}$ = 7.95 Hz, 1H, H5), 4.51 (m, 4H, H7), 4.22 (m, 4H, H8), 3.75 (s, 3H, H9), 3.74 (s, 3H, H9), 3.41 (s, 2H, H2), 1.55 (s, 6H, H1). ¹³C{¹H} NMR (126 MHz, CD₃CN): δ 165.66, 162.34, 148.93, 148.79, 148.35, 147.64, 128.48, 128.02, 121.20, 121.03, 119.86, 119.69, 117.04, 116.96, 72.21, 71.92, 70.61, 68.73, 68.35, 68.14, 62.22, 62.05, 25.31. ¹⁹F NMR (470 MHz, CD₃CN): δ -79.88. Anal. Calcd for C₂₇H₃₀N₂O₁₅F₉S₃NiLa ([Ni,La]^T): C, 29.88; H, 2.79; N, 2.58. Found: C, 29.83; H, 2.92; N, 2.60. Cyclic voltammetry (0.1 M [nBu₄N]⁺[PF₆]⁻ in CH₃CN): $E_{1/2}$ = -1.42 V vs Fc^{+/-}. Electronic absorption spectrum in CH₃CN (M⁻¹ cm⁻¹): 375 (4354) nm.

[Ni,Lu]^T. Yield: 100%. ¹H NMR (500 MHz, CD₃CN): δ 7.85 (s, 1H, H3), 7.84 (s, 1H, H3), 7.33 (d, $^3J_{H,H}$ = 8.05 Hz, 1H, H4), 7.25 (d, $^3J_{H,H}$ = 7.95 Hz, 3H, H4 H6), 6.97 (t, $^3J_{H,H}$ = 7.90 Hz, 1H, H5), 6.95 (t, $^3J_{H,H}$ = 7.95 Hz, 1H, H5), 4.57 (m, 4H, H7), 4.17 (m, 4H, H8), 3.74 (s, 3H, H9), 3.73 (s, 3H, H9), 3.40 (s, 2H, H2), 1.55 (s, 6H, H1). ¹³C{¹H} NMR (126 MHz, CD₃CN): δ 165.20, 162.00, 147.91, 147.86, 147.42, 128.87, 128.38, 121.63, 121.38, 120.16, 120.07, 117.90, 72.53, 72.50, 70.73, 69.47, 69.33, 69.27, 62.96, 62.86, 25.24. ¹⁹F NMR (470 MHz, CD₃CN): δ -79.98. Anal. Calcd for C₂₇H₃₀N₂O₁₅F₉S₃NiLu ([Ni,Lu]^T): C, 28.87; H, 2.69; N, 2.49. Found: C, 28.61; H, 2.99; N, 2.48. Cyclic voltammetry (0.1 M [nBu₄N]⁺[PF₆]⁻ in CH₃CN): $E_{1/2}$ = -1.43 V vs Fc^{+/-}. Electronic absorption spectrum in CH₃CN (M⁻¹ cm⁻¹): 374 (4302) nm.

ASSOCIATED CONTENT

Supporting Information

The Supporting Information is available free of charge at <https://pubs.acs.org/doi/10.1021/acs.inorgchem.4c03352>.

NMR spectra, characterization data for the complexes reported in this work, electrochemical data and related analysis, and detailed information regarding the XRD analysis (PDF)

Cartesian coordinates for the XRD structures (XYZ)

Accession Codes

Deposition Numbers 2323322–2323327 contain the supplementary crystallographic data for this paper. These data can be obtained free of charge via the joint Cambridge Crystallographic Data Centre (CCDC) and Fachinformationszentrum Karlsruhe Access Structures service.

AUTHOR INFORMATION

Corresponding Author

James D. Blakemore – Department of Chemistry, University of Kansas, Lawrence, Kansas 66045, United States;

ORCID: [0000-0003-4172-7460](https://orcid.org/0000-0003-4172-7460); Email: blakemore@ku.edu

Authors

Joseph P. Karnes – Department of Chemistry, University of Kansas, Lawrence, Kansas 66045, United States

Natalie M. Lind – Department of Chemistry, University of Kansas, Lawrence, Kansas 66045, United States

Allen G. Oliver – Department of Chemistry and Biochemistry, University of Notre Dame, Notre Dame, Indiana 46556, United States; ORCID: [0000-0002-0511-1127](https://orcid.org/0000-0002-0511-1127)

Cynthia S. Day – Department of Chemistry, Wake Forest University, Winston-Salem, North Carolina 27109, United States

Victor W. Day – Department of Chemistry, University of Kansas, Lawrence, Kansas 66045, United States

Complete contact information is available at: <https://pubs.acs.org/10.1021/acs.inorgchem.4c03352>

Author Contributions

The manuscript was written through contributions of all authors. All authors have given approval to the final version of the manuscript.

Notes

The authors declare no competing financial interest.

ACKNOWLEDGMENTS

This work was supported by the U.S. Department of Energy, Office of Science, Office of Basic Energy Sciences, through the Early Career Research Program (DE-SC0019169). J.P.K. was supported by a U.S. National Science Foundation Research Traineeship (NRT) at the University of Kansas (DGE-1922649). X-ray facilities at Wake Forest University were supported by the U.S. National Science Foundation through Award CHE-0234489. A preprint reflecting a preliminary version of the findings reported here was posted to a preprint server.⁵⁵

REFERENCES

- 1) Tsui, E. Y.; Agapie, T. Reduction potentials of heterometallic manganese-oxido cubane complexes modulated by redox-inactive metals. *Proc. Nat. Acad. Sci. U.S.A.* **2013**, *110*, 10084–10088.

(2) (a) Park, Y. J.; Ziller, J. W.; Borovik, A. S. The Effects of Redox-Inactive Metal Ions on the Activation of Dioxygen: Isolation and Characterization of a Heterobimetallic Complex Containing a Mn^{III} -(μ -OH)- Ca^{II} Core. *J. Am. Chem. Soc.* **2011**, *133*, 9258–9261. (b) Lacy, D. C.; Park, Y. J.; Ziller, J. W.; Yano, J.; Borovik, A. S. Assembly and Properties of Heterobimetallic $Co^{II/III}/Ca^{II}$ Complexes with Aquo and Hydroxo Ligands. *J. Am. Chem. Soc.* **2012**, *134*, 17526–17535.

(3) Reath, A. H.; Ziller, J. W.; Tsay, C.; Ryan, A. J.; Yang, J. Y. Redox Potential and Electronic Structure Effects of Proximal Nonredox Active Cations in Cobalt Schiff Base Complexes. *Inorg. Chem.* **2017**, *56*, 3713–3718.

(4) Kumar, A.; Lionetti, D.; Day, V. W.; Blakemore, J. D. Redox-Inactive Metal Cations Modulate the Reduction Potential of the Uranyl Ion in Macrocyclic Complexes. *J. Am. Chem. Soc.* **2020**, *142*, 3032–3041.

(5) (a) Krogman, J. P.; Foxman, B. M.; Thomas, C. M. Activation of CO_2 by a Heterobimetallic Zr/Co Complex. *J. Am. Chem. Soc.* **2011**, *133*, 14582–14585. (b) Cooper, B. G.; Napoline, J. W.; Thomas, C. M. Catalytic Applications of Early/Late Heterobimetallic Complexes. *Catal. Rev.: Sci. Eng.* **2012**, *54*, 1–40.

(6) (a) Mazzacano, T. J.; Mankad, N. P. Base Metal Catalysts for Photochemical C-H Borylation That Utilize Metal-Metal Cooperativity. *J. Am. Chem. Soc.* **2013**, *135*, 17258–17261. (b) Mankad, N. P. Diverse bimetallic mechanisms emerging from transition metal Lewis acid/base pairs: development of co-catalysis with metal carbenes and metal carbonyl anions. *Chem. Commun.* **2018**, *54*, 1291–1302.

(7) Tran, T. V.; Karas, L. J.; Wu, J. I.; Do, L. H. Elucidating Secondary Metal Cation Effects on Nickel Olefin Polymerization Catalysts. *ACS Catal.* **2020**, *10*, 10760–10772.

(8) (a) Deacy, A. C.; Moreby, E.; Phanopoulos, A.; Williams, C. K. $Co^{(III)}/Alkali-Metal^{(I)}$ Heterodinuclear Catalysts for the Ring-Opening Copolymerization of CO_2 and Propylene Oxide. *J. Am. Chem. Soc.* **2020**, *142*, 19150–19160. (b) Lindeboom, W.; Fraser, D. A. X.; Durr, C. B.; Williams, C. K. Heterodinuclear $Zn^{(II)}$, $Mg^{(II)}$ or $Co^{(III)}$ with $Na^{(I)}$ Catalysts for Carbon Dioxide and Cyclohexene Oxide Ring Opening Copolymerizations. *Chem. - Eur. J.* **2021**, *27*, 12224–12231. (c) Diment, W. T.; Williams, C. K. Chain end-group selectivity using an organometallic $Al^{(III)}/K^{(I)}$ ring-opening copolymerization catalyst delivers high molar mass, monodisperse polyesters. *Chem. Sci.* **2022**, *13*, 8543–8549. (d) Fiorentini, F.; Diment, W. T.; Deacy, A. C.; Kerr, R. W. F.; Faulkner, S.; Williams, C. K. Understanding catalytic synergy in dinuclear polymerization catalysts for sustainable polymers. *Nat. Commun.* **2023**, *14*, 4783. (e) Shellard, E. J. K.; Diment, W. T.; Resendiz-Lara, D. A.; Fiorentini, F.; Gregory, G. L.; Williams, C. K. $Al^{(III)}/K^{(I)}$ Heterodinuclear Polymerization Catalysts Showing Fast Rates and High Selectivity for Polyester Polyols. *ACS Catal.* **2024**, *14*, 1363–1374.

(9) Liu, Y.; Lau, T.-C. Activation of Metal Oxo and Nitrido Complexes by Lewis Acids. *J. Am. Chem. Soc.* **2019**, *141*, 3755–3766.

(10) Ramirez, B. L.; Lu, C. C. Rare-Earth Supported Nickel Catalysts for Alkyne Semihydrogenation: Chemo- and Regioselectivity Impacted by the Lewis Acidity and Size of the Support. *J. Am. Chem. Soc.* **2020**, *142*, 5396–5407.

(11) Kuppuswamy, S.; Powers, T. M.; Krogman, J. P.; Bezpalko, M. W.; Foxman, B. M.; Thomas, C. M. Vanadium–iron complexes featuring metal–metal multiple bonds. *Chem. Sci.* **2013**, *4*, 3557–3565.

(12) Kumar, A.; Lionetti, D.; Day, V. W.; Blakemore, J. D. Trivalent Lewis Acidic Cations Govern the Electronic Properties and Stability of Heterobimetallic Complexes of Nickel. *Chem. Eur. J.* **2018**, *24*, 141–149.

(13) Soto, M. A.; Carta, V.; Cano, M. T.; Andrews, R. J.; Patrick, B. O.; MacLachlan, M. J. Multiresponsive Cyclometalated Crown Ether Bearing a Platinum(II) Metal Center. *Inorg. Chem.* **2022**, *61*, 2999–3006.

(14) Kang, K.; Fuller, J.; Reath, A. H.; Ziller, J. W.; Alexandrova, A. N.; Yang, J. Y. Installation of internal electric fields by non-redox active cations in transition metal complexes. *Chem. Sci.* **2019**, *10*, 10135–10142.

(15) Miller, A. J. M. Controlling ligand binding for tunable and switchable catalysis: cation-modulated hemilability in pincer-crown ether ligands. *Dalton Trans.* **2017**, *46*, 11987–12000.

(16) (a) Cai, Z.; Xiao, D.; Do, L. H. Fine-Tuning Nickel Phenoxyimine Olefin Polymerization Catalysts: Performance Boosting by Alkali Cations. *J. Am. Chem. Soc.* **2015**, *137*, 15501–15510. (b) Cai, Z.; Do, L. H. Customizing Polyolefin Morphology by Selective Pairing of Alkali Ions with Nickel Phenoxyimine-Polyethylene Glycol Catalysts. *Organometallics* **2017**, *36*, 4691–4698. (c) Cai, Z.; Do, L. H. Thermally Robust Heterobimetallic Palladium–Alkali Catalysts for Ethylene and Alkyl Acrylate Copolymerization. *Organometallics* **2018**, *37*, 3874–3882. (d) Tran, T. V.; Nguyen, Y. H.; Do, L. H. Development of highly productive nickel–sodium phenoxyphosphine ethylene polymerization catalysts and their reaction temperature profiles. *Polymer Chem.* **2019**, *10*, 3718–3721. (e) Xiao, D.; Cai, Z.; Do, L. H. Accelerating ethylene polymerization using secondary metal ions in tetrahydrofuran. *Dalton Trans.* **2019**, *48*, 17887–17897.

(17) Lionetti, D.; Suseno, S.; Shiau, A. A.; de Ruiter, G.; Agapie, T. Redox Processes Involving Oxygen: The Surprising Influence of Redox-Inactive Lewis Acids. *JACS Au* **2024**, *4*, 344–368.

(18) (a) Van Staveren, C. J.; Van Eerden, J.; Van Veggel, F. C. J. M.; Harkema, S.; Reinhoudt, D. N. Cocomplexation of neutral guests and electrophilic metal cations in synthetic macrocyclic hosts. *J. Am. Chem. Soc.* **1988**, *110*, 4994–5008. (b) Van Veggel, F. C. J. M.; Harkema, S.; Bos, M.; Verboom, W.; Van Staveren, C. J.; Gerritsma, G. J.; Reinhoudt, D. N. Metallomacrocycles: synthesis, x-ray structure, electrochemistry, and ESR spectroscopy of mononuclear and heterodinuclear complexes. *Inorg. Chem.* **1989**, *28*, 1133–1148.

(19) (a) Chantarojsiri, T.; Reath, A. H.; Yang, J. Y. Cationic Charges Leading to an Inverse Free-Energy Relationship for N–N Bond Formation by Mn^{VI} Nitrides. *Angew. Chem., Int. Ed.* **2018**, *57*, 14037–14042. (b) Chantarojsiri, T.; Ziller, J. W.; Yang, J. Y. Incorporation of redox-inactive cations promotes iron catalyzed aerobic C–H oxidation at mild potentials. *Chem. Sci.* **2018**, *9*, 2567–2574.

(20) Dopp, C. M.; Golwankar, R. R.; Kelsey, S. R.; Douglas, J. T.; Erickson, A. N.; Oliver, A. G.; Day, C. S.; Day, V. W.; Blakemore, J. D. Vanadyl as a Spectroscopic Probe of Tunable Ligand Donor Strength in Bimetallic Complexes. *Inorg. Chem.* **2023**, *62*, 9827–9843.

(21) Nguyen, H. M.; Morgan, H. W. T.; Chantarojsiri, T.; Kerr, T. A.; Yang, J. Y.; Alexandrova, A. N.; Léonard, N. G. Charge and Solvent Effects on the Redox Behavior of Vanadyl Salen–Crown Complexes. *J. Phys. Chem. A* **2023**, *127*, 5324–5334.

(22) Karnes, J. P.; Kumar, A.; Hopkins Leseberg, J. A.; Day, V. W.; Blakemore, J. D. Trivalent Cations Slow Electron Transfer to Macrocyclic Heterobimetallic Complexes. *Inorg. Chem.* **2024**, *63*, 8710–8729.

(23) Golwankar, R. R.; Kumar, A.; Day, V. W.; Blakemore, J. D. Revealing the Influence of Diverse Secondary Metal Cations on Redox-Active Palladium Complexes. *Chem. Eur. J.* **2022**, *28*, No. e202200344.

(24) Golwankar, R. R.; Ervin, A. C.; Makoś, M. Z.; Mikeska, E. R.; Glezakou, V.-A.; Blakemore, J. D. Synthesis, Isolation, and Study of Heterobimetallic Uranyl Crown Ether Complexes. *J. Am. Chem. Soc.* **2024**, *146*, 9597–9604.

(25) Milburn, G. H. W.; Truter, M. R.; Vickery, B. L. The crystal structure of a sodium complex, sodium perchlorate–bis-[NN'-ethylenebis(salicylideneiminato)copper(II)]. *Chem. Commun.* **1968**, *0*, 1188–1188.

(26) Maity, S.; Ghosh, S.; Ghosh, A. Elucidating the secondary effect in the Lewis acid mediated anodic shift of electrochemical oxidation of a $Cu^{(II)}$ complex with a N_2O_2 donor unsymmetrical ligand. *Dalton Trans.* **2019**, *48*, 14898–14913.

(27) (a) Ghosh, T. K.; Mahapatra, P.; Drew, M. G. B.; Franconetti, A.; Frontera, A.; Ghosh, A. The Effect of Guest Metal Ions on the Reduction Potentials of Uranium(VI) Complexes: Experimental and Theoretical Investigations. *Chem. Eur. J.* **2020**, *26*, 1612–1623.

(b) Ghosh, T. K.; Maity, S.; Ghosh, S.; Gomila, R. M.; Frontera, A.; Ghosh, A. Role of Redox-Inactive Metal Ions in Modulating the Reduction Potential of Uranyl Schiff Base Complexes: Detailed Experimental and Theoretical Studies. *Inorg. Chem.* **2022**, *61*, 7130–7142. (c) Bhunia, P.; Gomila, R. M.; Frontera, A.; Ghosh, A. Combined effects of the Lewis acidity and electric field of proximal redox innocent metal ions on the redox potential of vanadyl Schiff base complexes: an experimental and theoretical study. *Dalton Trans.* **2023**, *52*, 3097–3110.

(28) Lo, W.-K.; Wong, W.-K.; Guo, J.; Wong, W.-Y.; Li, K.-F.; Cheah, K.-W. Synthesis, structures and luminescent properties of new heterobimetallic Zn-4f Schiff base complexes. *Inorg. Chim. Acta* **2004**, *357*, 4510–4521.

(29) Nayak, M.; Jana, A.; Fleck, M.; Hazra, S.; Mohanta, S. A unique example of a three component cocrystal of metal complexes. *CrystEngComm* **2010**, *12*, 1416–1421.

(30) Sarkar, S.; Mohanta, S. Syntheses, crystal structures and supramolecular topologies of nickel(II)-s/p/d¹⁰/NH₄⁺ complexes derived from a compartmental ligand. *RSC Adv.* **2011**, *1*, 640–650.

(31) Sarr, M.; Diop, M.; Thiam, I. E.; Gaye, M.; Barry, A. H.; Alvarez, N.; Ellena, J. Co-crystal structure of a dinuclear (Zn-Y) and a trinuclear (Zn-Y-Zn) complexes derived from a Schiff base ligand. *Eur. J. Chem.* **2018**, *9*, 67–73.

(32) Costes, J.-P.; Dahan, F.; Dupuis, A.; Laurent, J.-P. A Genuine Example of a Discrete Bimetallic (Cu, Gd) Complex: Structural Determination and Magnetic Properties. *Inorg. Chem.* **1996**, *35*, 2400–2402.

(33) Shao, H.; Muduli, S. K.; Tran, P. D.; Soo, H. S. Enhancing electrocatalytic hydrogen evolution by nickel salicylaldimine complexes with alkali metal cations in aqueous media. *Chem. Commun.* **2016**, *52*, 2948–2951.

(34) Ghosh, D.; Febriansyah, B.; Gupta, D.; Ng, L. K.-S.; Xi, S.; Du, Y.; Baikie, T.; Dong, Z.; Soo, H. S. Hybrid Nanomaterials with Single-Site Catalysts by Spatially Controllable Immobilization of Nickel Complexes via Photoclick Chemistry for Alkene Epoxidation. *ACS Nano* **2018**, *12*, 5903–5912.

(35) Ho, X. L.; Shao, H.; Ng, Y. Y.; Ganguly, R.; Lu, Y.; Soo, H. S. Visible Light Driven Hydrogen Evolution by Molecular Nickel Catalysts with Time-Resolved Spectroscopic and DFT Insights. *Inorg. Chem.* **2019**, *58*, 1469–1480.

(36) Eisenhardt, K. H. S.; Fiorentini, F.; Lindeboom, W.; Williams, C. K. Quantifying CO₂ Insertion Equilibria for Low-Pressure Propene Oxide and Carbon Dioxide Ring Opening Copolymerization Catalysts. *J. Am. Chem. Soc.* **2024**, *146*, 10451–10464.

(37) Schall, O. F.; Robinson, K.; Atwood, J. L.; Gokel, G. W. Self-assembling nickel clusters form binding sites for alkali metal cations: novel analogs of enolate aggregates. *J. Am. Chem. Soc.* **1993**, *115*, 5962–5969.

(38) Park, D.; Jette, C. I.; Kim, J.; Jung, W.-O.; Lee, Y.; Park, J.; Kang, S.; Han, M. S.; Stoltz, B. M.; Hong, S. Enantioselective Alkynylation of Trifluoromethyl Ketones Catalyzed by Cation-Binding Salen Nickel Complexes. *Angew. Chem., Int. Ed.* **2020**, *59*, 775–779.

(39) Perrin, D. D. Tables. In *Ionization Constants of Inorganic Acids and Bases in Aqueous Solution*, 2nd ed. Perrin, D. D., Ed.; Pergamon, 1982; pp 1–138.

(40) The occupancy factors of the secondary cations were determined through refinement to be as follows: K⁺, 0.97(1); Li⁺, 1.01(4); Sr²⁺, 1.01(1); Zn²⁺, 0.99(1); Lu³⁺, 1.00(1). The occupancy factors for the nickel centers in each corresponding complex were 0.99(1), 102(1), 99(1), 99(1), and 100(1).

(41) Shannon, R. D. Revised effective ionic radii and systematic studies of interatomic distances in halides and chalcogenides. *Acta Crystallogr.* **1976**, *A32*, 751–767.

(42) Yang, L.; Powell, D. R.; Houser, R. P. Structural variation in copper(I) complexes with pyridylmethylamide ligands: structural analysis with a new four-coordinate geometry index, $\tau 4$. *Dalton Trans.* **2007**, 955–964.

(43) Pauling, L. *The Nature of the Chemical Bond*; Cornell University Press: Ithaca, NY, 1960; p 244.

(44) Kelsey, S. R.; Kumar, A.; Oliver, A. G.; Day, V. W.; Blakemore, J. D. Promotion and Tuning of the Electrochemical Reduction of Hetero- and Homobimetallic Zinc Complexes. *ChemElectroChem.* **2021**, *8*, 2750–2751.

(45) Golwankar, R. R.; Curry, T. D., II; Paranjothi, C. J.; Blakemore, J. D. Molecular Influences on the Quantification of Lewis Acidity with Phosphine Oxide Probes. *Inorg. Chem.* **2023**, *62*, 9765–9780.

(46) Kumar, A.; Blakemore, J. D. On the Use of Aqueous Metal-Aqua pK_a Values as a Descriptor of Lewis Acidity. *Inorg. Chem.* **2021**, *60*, 1107–1115.

(47) (a) Kheradmandan, S.; Schmalle, H. W.; Jacobsen, H.; Blacque, O.; Fox, T.; Berke, H.; Gross, M.; Decurtins, S. An Unusual (10,3)-a Racemic Twofold Interpenetrating Network Assembled from Isolable Tris(cyclopentadienyl)manganate and Cesocene Building Blocks. *Chem. Eur. J.* **2002**, *8*, 2526–2533. (b) Kheradmandan, S.; Schmalle, H. W.; Jacobsen, H.; Blacque, O.; Fox, T.; Berke, H.; Gross, M.; Decurtins, S. An Unusual (10,3)-a Racemic Twofold Interpenetrating Network Assembled from Isolable Tris(cyclopentadienyl)manganate and Cesocene Building Blocks. CCDC 167740: *Experimental Crystal Structure Determination*; 2002. DOI: [10.5517/cc5mjz8](https://doi.org/10.5517/cc5mjz8). (c) Teng, W.; Ruhlandt-Senge, K. Syntheses and Structures of the First Heavy-Alkali-Metal Tris(trimethylsilyl)-germanides. *Chem. Eur. J.* **2005**, *11*, 2462–2470. (d) Teng, W.; Ruhlandt-Senge, K. CCDC 245382: *Experimental Crystal Structure Determination*; 2005. DOI: [10.5517/cc87bkc](https://doi.org/10.5517/cc87bkc). (e) Bader, J.; Neumann, B.; Stammmer, H.-G.; Ignat'ev, N.; Hoge, B. Metal-free dehydrogenation of tri- and diethylamine with (C₂F₅)₃PF₂. *J. Fluorine Chem.* **2018**, *207*, 12–17. (f) Bader, J.; Neumann, B.; Stammmer, H.-G.; Ignat'ev, N.; Hoge, B. CCDC 967082: *Experimental Crystal Structure Determination*; 2018. DOI: [10.5517/ccdc.csd.ccl1gb61](https://doi.org/10.5517/ccdc.csd.ccl1gb61). (g) Lirette, F.; Darvish, A.; Zhou, Z.; Wei, Z.; Renn, L.; Petrukhina, M. A.; Weitz, R. T.; Morin, J.-F. Dibenzannulated peri-acenoacenes from anthanthrene derivatives. *Chem. Sci.* **2023**, *14*, 10184–10193. (h) Lirette, F.; Darvish, A.; Zhou, Z.; Wei, Z.; Renn, L.; Petrukhina, M. A.; Weitz, R. T.; Morin, J.-F. CCDC 2266823: *Experimental Crystal Structure Determination*; 2023. DOI: [10.5517/ccdc.csd.cc2g2tbq](https://doi.org/10.5517/ccdc.csd.cc2g2tbq).

(48) Bard, A. J.; Faulkner, L. R. *Electrochemical Methods: Fundamentals and Applications*, 2nd ed.; Wiley: Hoboken, NJ, 2001.

(49) Savéant, J. M.; Costentin, C. *Elements of Molecular and Biomolecular Electrochemistry, An Electrochemical Approach to Electron Transfer Chemistry*, 2nd ed.; Wiley: Hoboken, NJ, 2019; p 616.

(50) (a) Manzur, C.; Bustos, C.; Schrebler, R.; Carrillo, D.; Knobler, C. B.; Gouzerh, P.; Jeannin, Y. Synthesis, characterization and electrochemistry of nickel(II) complexes of Schiff base ligands containing a disulphide group. Crystal structure of [Ni{-(o-OC₆H₄CH-NC₆H₄)₂S₂}](MeOH)]. · MeOH. *Polyhedron* **1989**, *8*, 2321–2330. (b) Chiang, L.; Kochem, A.; Jarjales, O.; Dunn, T. J.; Vezin, H.; Sakaguchi, M.; Ogura, T.; Orio, M.; Shimazaki, Y.; Thomas, F.; Storr, T. Radical Localization in a Series of Symmetric NiII Complexes with Oxidized Salen Ligands. *Chem. Eur. J.* **2012**, *18*, 14117–14127. (c) Chiang, L.; Herasymchuk, K.; Thomas, F.; Storr, T. Influence of Electron-Withdrawing Substituents on the Electronic Structure of Oxidized Ni and Cu Salen Complexes. *Inorg. Chem.* **2015**, *54*, 5970–5980.

(51) Falivene, L.; Credendino, R.; Poater, A.; Petta, A.; Serra, L.; Oliva, R.; Scarano, V.; Cavallo, L. SambVca 2. A Web Tool for Analyzing Catalytic Pockets with Topographic Steric Maps. *Organometallics* **2016**, *35*, 2286–2293.

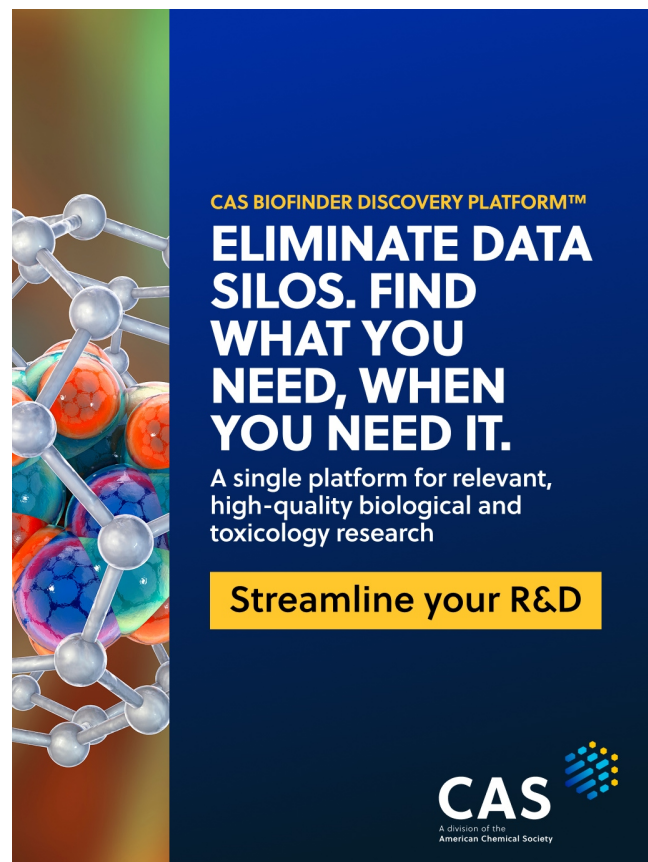
(52) (a) Poater, A.; Ragone, F.; Giudice, S.; Costabile, C.; Dorta, R.; Nolan, S. P.; Cavallo, L. Thermodynamics of N-Heterocyclic Carbene Dimerization: The Balance of Sterics and Electronics. *Organometallics* **2008**, *27*, 2679–2681. (b) Poater, A.; Ragone, F.; Mariz, R.; Dorta, R.; Cavallo, L. Comparing the Enantioselective Power of Steric and Electrostatic Effects in Transition-Metal-Catalyzed Asymmetric Synthesis. *Chem. Eur. J. Int. Ed.* **2010**, *16*, 14348–14353. (c) Falivene, L.; Cao, Z.; Petta, A.; Serra, L.; Poater, A.; Oliva, R.; Scarano, V.; Cavallo,

L. Towards the online computer-aided design of catalytic pockets. *Nat. Chem.* **2019**, *11*, 872–879.

(53) The differences in the free volumes about the nickel centers in the relevant pairs of tiara and crown complexes appear rather small. Nonetheless, as the trends among all the data are sensible and can be readily interpreted in the context of the structural analyses presented in this report and in our prior report,²² we anticipate that the differences in free volumes are significant. One major potential source of uncertainty in the free-volume analysis is the possibility of changes in the structures of the complexes upon dissolution in solvent/electrolyte; structural change upon dissolution appears likely for, at least, $[\text{Ni},\text{K}]^T$ (see the SI, p S88, for discussion). Additionally, some aspects of the SambVca computational method, particularly regarding treatment of hydrogen atoms, could lead to uncertainty in the results. In our work, the structures that were loaded into SambVca for analysis had all hydrogen atoms included, but at locations determined by riding models during refinement of the XRD data; no computational methods were used to minimize the energies of the structures. However, on the basis of the structural similarity of the two co-crystallized isomers of $[\text{Ni},\text{Lu}]^T$ that occupy different volumes of the asymmetric unit of structure jk1138 (Figure S166), we anticipate that our structures are representative of low energy forms of the compounds. Readers are suggested to refer to the Supporting Information document provided with our prior work²² on pp S103–S106 for a more robust discussion of the computational settings in SambVca and their possible impacts on the results of free-volume analyses of the type reported here.

(54) Nicholson, R. S. Theory and Application of Cyclic Voltammetry for Measurement of Electrode Reaction Kinetics. *Anal. Chem.* **1965**, *37*, 1351–1355.

(55) Karnes, J.; Oliver, A.; Day, C.; Day, V.; Blakemore, J. Tunability in Heterobimetallic Complexes Featuring an Acyclic “Tiara” Polyether Motif. *ChemRxiv (Inorg. Chem.)* **2024**, DOI: 10.26434/chemrxiv-2024-p6wg1.



CAS BIOFINDER DISCOVERY PLATFORM™

ELIMINATE DATA SILOS. FIND WHAT YOU NEED, WHEN YOU NEED IT.

A single platform for relevant, high-quality biological and toxicology research

Streamline your R&D

CAS A division of the American Chemical Society